Results in Optics 24 (2026) 101049

Contents lists available at ScienceDirect

Results in Optics

journal homepage: www.sciencedirect.com/journal/results-in-optics

Plasmonic photonic synapse with spectral bipolar weight control and ultra-low energy consumption using GST material

Ozra Sharifipour, Parviz Keshavarzi, Mohammad Danaie *

Faculty of Electrical and Computer Engineering, Semnan University, Semnan, Iran

ARTICLE INFO

Keywords:
Phase-change material
Plasmonicnano-ring resonator
Neuromorphic
Nanophononics
Spiking-timing-dependent plasticity (STDP)
Synapse

ABSTRACT

Neuromorphic photonic systems have emerged as a promising platform for overcoming the bandwidth and energy limitations of conventional electronic neural networks, where the realization of compact, low-power, and non-volatile synaptic elements remains a key challenge. In this work, an all-optical plasmonic nano-synapse is proposed for energy-efficient neuromorphic photonic architectures. The device is based on a nanoscale plasmonic ring resonator orthogonally coupled to two independent waveguides, enabling physically separated data transmission and optical control. A nanometric $Ge_2Sb_2Te_5$ (GST) phase-change layer is integrated at the coupling region between the resonator and the data waveguide, allowing non-volatile, multi-level modulation of synaptic weights through resonance wavelength tuning. Unlike conventional photonic synapses that primarily support unipolar weight modulation, the proposed architecture enables bipolar synaptic weight control within a single compact device by operating on opposite sides of the resonance wavelength, corresponding to excitatory and inhibitory synaptic responses. This spectral-domain weight encoding provides a robust alternative to time-domain spiking schemes and enables spike-timing-dependent plasticity (STDP)-compatible weight updates while significantly reducing circuit complexity. Numerical simulations demonstrate an ultra-compact footprint of approximately 0.09 μm^2, an active GST volume below 5×10^{-5} μm^3, and an ultra-low optical switching energy of about 5 pJ. The use of a low-loss silver-based plasmonic platform combined with air cladding results in strong field confinement and an optical contrast approaching 99%. Owing to its compact size, non-volatility, and spectral bipolar weight capability, the proposed plasmonic synapse offers a scalable and practical building block for high-density, low-power neuromorphic photonic processors.

1. Introduction

In recent years, neuromorphic architectures inspired by the structure and function of the human brain have been increasingly implemented on electronic platforms. These architectures aim to emulate features such as learning, adaptability, and parallel processing by utilizing integrated circuits, CMOS transistors, and memristors. For instance, IBM's TrueNorth chip with more than one million neurons and hundreds of millions of synapses is a successful example that enables image processing and pattern recognition with extremely low power consumption (Merolla et al., 2014 Aug 8; Davies et al., 2018 Jan 16; Yang et al., 2013 Jan; Indiveri and Liu, 2015 Jul 15). Similarly, Intel's Loihi chip, which supports spiking-based algorithms and real-time learning, represents a major advancement in electronic neuromorphic systems (Furber, 2016 Aug 16; Benjamin et al., 2014 Apr 24; Fan et al., 2507). The use of memristors as programmable synapses has also provided the ability to store weights and emulate synaptic behavior (Strukov et al., 2008 May 1; Prezioso et al., 2015 May 7; Aguilera et al., 2020 Mar).

Despite these achievements, electronic neuromorphic systems face significant challenges. Scaling up the number of neurons and synapses results in a substantial increase in energy consumption and demands for memory and computational power (Marković et al., 2020 Sep 17; Shastri et al., 2021 Feb; Ahmadi et al., 2024 Dec 30). Moreover, the speed of electronic signal transmission and the physical limitations of silicon chips pose serious obstacles to large-scale parallel processing and scalability (Maass, 2016 Oct; Sze et al., 2020 Jun 16; Roy et al., 2019 Nov 28). Other issues such as electromagnetic interference, excessive heat generation, and reduced operational reliability are exacerbated with increasing device density (Boahen, 2017 Mar 15; Indiveri et al., 2011 May; Markovic, 2024). Collectively, these constraints hinder the performance and scalability of deep and large neural networks on electronic platforms.

* Corresponding author.
E-mail address: danaie@semnan.ac.ir (M. Danaie).

https://doi.org/10.1016/j.rio.2026.101049
Received 3 October 2025; Received in revised form 10 May 2026; Accepted 16 May 2026
Available online 22 May 2026

To overcome these limitations, optical neuromorphic technologies have been proposed as innovative solutions (Cheng et al., 2017 Sep 27; Nohoji et al., 2024 May; Song et al., 2022 Aug 3). Unlike electrons, photons are used for information transmission and processing, offering remarkable advantages including significantly higher speed, ultra-low latency, reduced power consumption, and enhanced robustness against electromagnetic noise (Brückerhoff-Plückelmann et al., 2023 Oct; Prucnal and Shastri, 2017 May 8). Additionally, the ability to employ multiple wavelengths simultaneously for data transmission improves system scalability and flexibility compared to electronic approaches (Miller, 2010 Jan; Giamougiannis et al., 2022). Consequently, optical neuromorphic computing emerges as an efficient and promising strategy for realizing high-speed, low-power, and large-scale neural networks (Shastri et al., 2021; Soref, 2007 Mar 5).

Silicon photonics has recently become a central platform for developing optical neuromorphic systems. Its key advantages include full compatibility with standard CMOS fabrication processes, low-cost mass production, thermal stability, integration capability with electronic components, and very high data transmission rates (Tsakyridis et al., 2022; Shen et al., 2017 Jul 1; Maier, 2007). These benefits have led to widespread applications of silicon photonics in integrated optical circuits, optical neural networks, and neuromorphic sensors.

Various implementations of artificial neurons and synapses using silicon photonics have been reported, such as programmable optical synapses based on silicon modulators, optical neural networks employing silicon waveguides, and artificial neurons realized via silicon ring resonators (Ozbay, 2006; Gramotnev and Bozhevolnyi, 2010 Feb; Brongersma et al., 2015 Jan; Boltasseva and Atwater, 2011 Jan 21). Furthermore, optical neuromorphic processors containing thousands of silicon-based neurons and synapses have been developed for high-speed parallel data processing (Anker et al., 2008 Jun; Wuttig et al., 2017 Aug 1). Silicon-based optical synapses provide programmable weighting and nonlinear functionalities that replicate biological synaptic responses (Ríos et al., 2015 Nov; Feldmann et al., 2019 May 9).

Nevertheless, silicon photonics entails inherent challenges. The most significant limitation is the diffraction limit, which restricts device miniaturization and integration density due to relatively large component sizes (Zhang et al., 2019 Mar; Rudé et al., 2015 Jun 17). Additionally, silicon's indirect bandgap inhibits its use for active optical sources, such as lasers and optical amplifiers, necessitating complementary or hybrid materials (Salinga et al., 2018 Aug; Zhang et al., 2018 Jan 1; Tame et al., 2013 Jun; Ambrogio et al., 2018 Jun 7). High energy consumption of silicon modulators and optical losses from scattering and absorption further reduce overall system efficiency (Xu et al., 2020 Dec; Tait et al., 2017 Aug 7). Additional constraints include temperature sensitivity, lack of intrinsic high-speed electro-optic modulation, and integration challenges with emerging materials and technologies such as phase-change materials and plasmonic (Shastri et al., 2021 Feb; Li et al., 2022 Jul).

In this context, plasmonic nanostructures have been attracting growing interest as a novel solution. Exploiting the unique physics of surface plasmon resonances collective oscillations of free electrons at metal-dielectric interfaces plasmonic structures can confine electromagnetic energy to volumes far smaller than the diffraction limit (Miller, 2009 Jun 10; Wright et al., 2013 May 13; Zhang et al., 2019 Sep 30). This enables ultra-compact optical components and greatly enhanced light-matter interactions. Surface plasmon polariton propagation at metal-dielectric boundaries allows nanoscale control of optical signals, making plasmonic devices highly attractive for next-generation interconnects, modulators, and optical switches (Hosseini et al., 2014 Jul 10; Stegmaier et al., 2017 Jan). Plasmonic optical switches benefit from high environmental sensitivity and the capability to modulate light intensity and phase, resulting in faster switching, reduced footprint, and improved performance. Moreover, plasmonic filters with high spectral selectivity and tunable transmission, along with highly sensitive plasmonic sensors, have found widespread applications in optical communications, signal processing, and biochemical as well as environmental sensing (Soref, 2007 Mar 5; Erickson et al., 2022 Apr 8; Sabella, 2019 Oct 24).

The strong electromagnetic field enhancement at plasmonic hotspots facilitates stronger nonlinear effects, higher sensitivity, and faster switching speeds (Tittl et al., 2018 Jun 8; Yoo et al., 2023 Oct). However, practical implementation of plasmonic devices is challenged by ohmic losses in metals and the scarcity of effective, non-volatile modulation mechanisms (Wang et al., 2016 Jan; Li et al., 2016 Aug). Most existing plasmonic switches are volatile, requiring continuous energy input to maintain their state, which is incompatible with the demands of large-scale neuromorphic and memory systems.

A transformative solution has arisen with phase-change materials, particularly Ge2Sb2Te5 (GST). GST is a chalcogenide compound that reversibly switches between amorphous and crystalline phases upon application of fast electrical or optical pulses (Gholipour et al., 2013 Apr 29; Farmakidis et al., 2022 Jul; Li, 2016). Each phase exhibits distinct optical and electrical properties, enabling dynamic, high-contrast optical modulation with extremely low energy consumption. The amorphous phase of GST features a disordered atomic structure, lower refractive index, and higher optical bandgap, whereas the crystalline phase has an ordered lattice, higher refractive index, and lower bandgap. These phase transitions occur on nanosecond time scales and remain stable at room temperature, making GST ideal for non-volatile data storage and optical switching (Wuttig et al., 2017 Aug 1; Gholipour et al., 2013 Apr 29).

Despite these advantages, integrating GST with conventional silicon waveguides is limited by weak overlap between the optical field and the phase-change material, resulting in modest modulation depth and device efficiency. However, combining GST with plasmonic nanostructures opens new avenues (Ríos et al., 2015 Nov; Zhang et al., 2019 Mar; Wu et al., 2018 Dec 19). The strong field confinement at plasmonic hotspots maximizes the interaction between even a thin GST layer and the optical field, greatly enhancing modulation contrast between amorphous and crystalline states (Rudé et al., 2015 Jun 17; Salinga et al., 2018 Aug). This synergy enables ultra-compact, energy-efficient, and reprogrammable optical devices essential for scalable neuromorphic hardware (Tame et al., 2013 Jun; Xu et al., 2019 Jan 7). For instance, a plasmonic resonator loaded with GST can function as a non-volatile optical switch or synaptic weight, consuming orders of magnitude less switching energy than all-silicon platforms. The strong field enhancement also supports multi-level (analog) modulation, emulating the variable weights of biological synapses an important factor for advanced neural network architectures (Ambrogio et al., 2018 Jun 7; Sharifipour et al., 2025 Jun; Sharifipour et al., 2025 May 31). Furthermore, the broadband optical contrast of GST combined with the spectral tunability of plasmonic resonators enables multi-wavelength operation, enhancing the density and performance of optical neural networks (Xu et al., 2020 Dec; Tait et al., 2017 Aug 7; Feldmann et al., 2021 Jan 7).

In this paper, we present an all-optical nanophotonic synapse based on the phase-change material GST and a plasmonic nanoscale ring resonator structure, which is orthogonally coupled to two waveguides for data and control signals, enabling precise and rapid modulation of the synaptic weight. The main innovation of this work lies in the capability to simultaneously implement bipolar synaptic weights both positive and negative—using a single integrated structure, achieved through spectral control and resonance wavelength tuning, applied in STDP learning.

This approach not only significantly reduces the hardware volume and complexity but also leads to considerable optimization in energy consumption (estimated to be around 5 picojoules) and increases the integration density in practical neuromorphic photonic networks. Moreover, the proposed structure, with an ultra-compact footprint of approximately 0.09 μm^2, a very limited active GST volume, and achieving a very high optical contrast (close to 99%), ensures reliable, fast, and low-power operation.

Given the advancements attained in this study, this synapse represents a milestone in the design and development of neuromorphic photonic systems featuring high throughput, low energy consumption, and multi-level, multi-parameter learning capability, which can play a key role in advanced and complex future information processing.

To address these limitations and build upon the recent advances in plasmonic and phase-change photonic architectures, this work proposes an ultra-compact all-optical plasmonic synapse that enables non-volatile, multi-level, and spectrally encoded bipolar weight control within a single device. The proposed design leverages a nanoscale plasmonic ring resonator with orthogonal coupling paths to physically separate data transmission from optical control, while a nanometric GST layer integrated at the coupling region enables efficient resonance tuning with extremely low switching energy. Unlike previously reported photonic synapses that mainly support unipolar or time-domain weight modulation, our architecture provides a novel spectral-domain approach in which excitatory and inhibitory weights naturally emerge on opposite sides of the resonance. This unique capability, combined with an active GST volume below 5×10^{-5} μm^3 and switching energies around 5 pJ, results in a practical and scalable building block for high-density neuromorphic photonic processors.

2. Background

This section establishes the theoretical foundation for the proposed plasmonic nano-synapse, bridging neuromorphic computing principles with the material properties of GST for optical synapses.

2.1. Spiking Neural Networks (SNNs) and Synaptic plasticity

Spiking Neural Networks (SNNs), the third generation of artificial neural networks, provide event-driven, temporally discrete processing, which significantly reduces energy consumption while maintaining high temporal precision (Nunes et al., 2022 Jun). The human brain contains approximately 86 billion neurons and more than 100 trillion synapses, each playing a crucial role in learning and adaptation. Fig. 1a illustrates a biological neuron, highlighting dendrites (which collect incoming signals), the soma (which integrates signals), and the axon (which transmits processed signals to other neurons). In contrast, Fig. 1b depicts an artificial neuron model inspired by its biological counterpart.

This model includes a set of weighted inputs x_i with corresponding synaptic weights w_i, to which a bias b is added. The sum is then passed through a nonlinear activation function $f(\cdot)$ to produce the neuron's output. This mathematical model forms the basis for both artificial neural networks and spiking neural networks:

$$y = \mathscr{F}\left(\sum_{i=1}^{N} \omega_i x_i + b\right) \quad (1)$$

Unlike ANNs that transmit information continuously, SNNs use discrete timed spikes, enabling closer biological plausibility and significant energy efficiency improvement (Pfeiffer and Pfeil, 2018 Oct). Fig. 2a depicts the weighted spike transmission and thresholding of postsynaptic neuron membrane potential.

A key learning mechanism in SNNs is Spike Timing Dependent Plasticity (STDP), where if the presynaptic spike precedes the postsynaptic spike, synaptic weight is potentiated (LTP); conversely, if it follows, the weight is depressed (LTD) (Zhang et al., 2020 Jun 16). Spike Timing Dependent Plasticity (STDP) provides a learning mechanism where presynaptic spike timing relative to postsynaptic spikes potentiates or depresses synaptic weights (Fig. 2b). The physical propagation of spikes through synapses, shown in Fig. 2c, underpins event-driven learning in both biological and artificial spiking systems (Wang et al., 2018 Feb).

Neuromorphic hardware implementations leverage non-volatile materials, including memristors and phase-change materials (PCMs) such as GST, to store multilevel synaptic weights and support scalable, energy-efficient photonic and electronic training methods] (Neftci et al., 2019 Nov 5).

2.2. Phase-Change materials for plasmonic Synapses: Focus on $Ge_2Sb_2Te_5$ (GST)

Phase-change materials (PCMs) are characterized by rapid and reversible transitions between amorphous and crystalline phases, accompanied by a pronounced contrast in their refractive index. These properties make PCMs essential for implementing memory and neuromorphic photonic circuits (Fong et al., 2017 Sep 21). Among them, GST stands out due to its high switching speed (sub-10 ns) and optical stability (Rudé et al., 2013), enabling efficient, low-energy, and non-volatile optical modulation.

As illustrated in Fig. 3a, a thin GST layer integrated into a plasmonic waveguide can be switched between amorphous and crystalline phases using short optical pulses. The Reset process (crystalline → amorphous) involves melting followed by rapid quenching, which disrupts the ordered atomic network, producing a disordered amorphous structure with distinct bonding patterns, especially in Ge–Te and Te–Te bonds. The Set process (amorphous → crystalline) proceeds via controlled heating, allowing atomic ordering and nucleation, as shown in the staged energy profile in Fig. 3b. This atomic-scale rearrangement underpins the fast, energy-efficient, and repeatable phase transitions of GST.

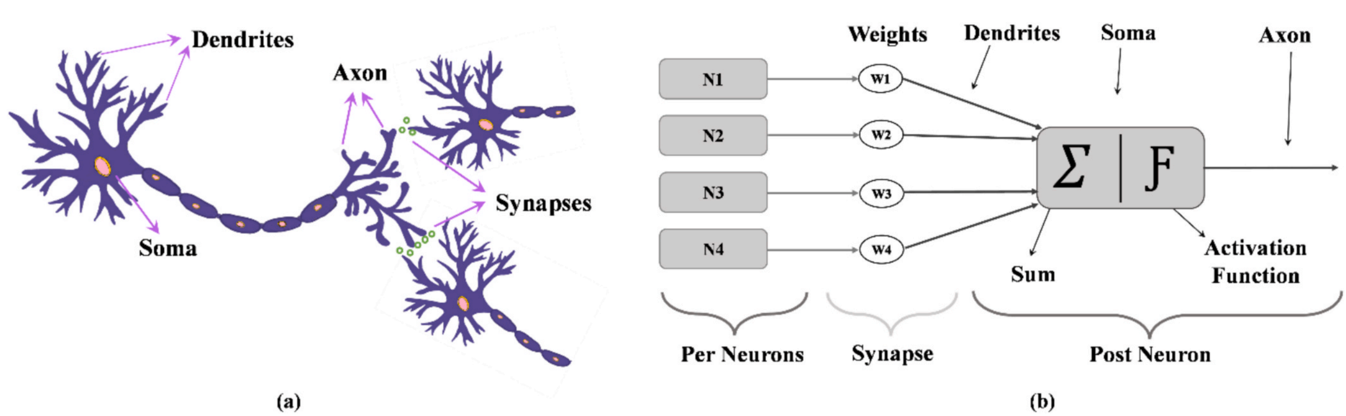

Fig. 1. Conceptual illustration of biological and artificial neurons. (a) Biological neuron consisting of dendrites, soma, and axon. (b) Generic artificial neuron model featuring weighted inputs, synaptic weights, bias, and a nonlinear activation function. These illustrations are provided solely for background purposes and do not depict the architecture, operation, or results of the proposed GST–plasmonic nano-synapse. No experimental or simulation data are represented.

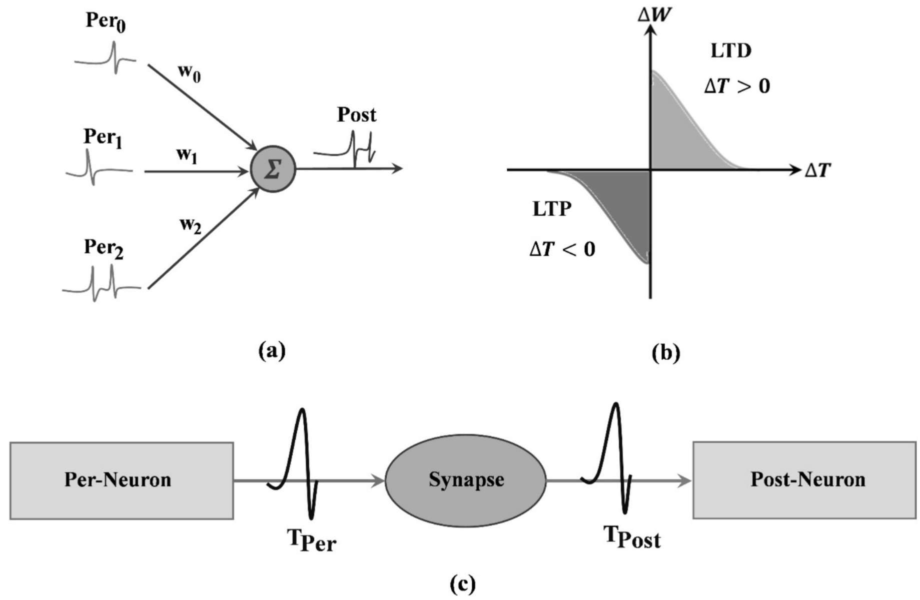

Fig. 2. Conceptual illustration of spike transmission and learning mechanisms in spiking neural networks. (a) Weighted presynaptic spike transmission and postsynaptic spike generation upon membrane potential thresholding. (b) Classical spike-timing-dependent plasticity (STDP) rule illustrating synaptic weight changes as a function of spike timing difference. (c) Physical representation of presynaptic and postsynaptic spike interactions. All panels are presented for conceptual background purposes only and are independent of the proposed device. No experimental or simulation data from this work are included.

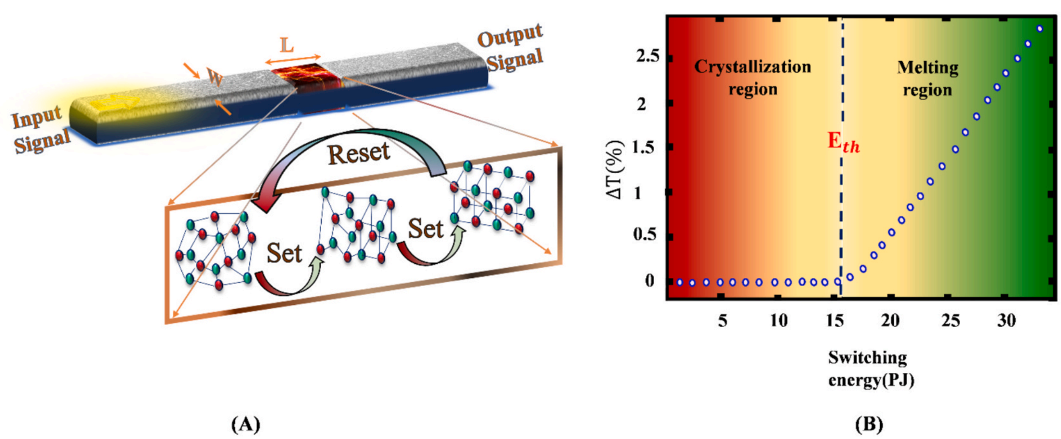

Fig. 3. Components of plasmonic waveguide with GST layer and its phase-change process. (a) Thin GST layer embedded in plasmonic waveguide switching between amorphous and crystalline states via optical pulses. (b) Energy profile and staged transition between amorphous and crystalline phases of GST.

The phase change directly affects the optical properties of the plasmonic structure. As the crystallization ratio of GST increases, the effective refractive index rises, producing a red-shift in the resonance wavelength and modulating transmission intensity around the resonance peak (Fig. 4). Fully amorphous and fully crystalline states represent the two extremes of transmission contrast, demonstrating the strong switching capability of GST-based devices.

Fig. 5 highlights the impact of GST phase on the electromagnetic field distribution within the resonator. In the amorphous phase, strong field confinement inside the resonator ensures efficient coupling with the waveguide, corresponding to a low-transmission ("OFF") state or near-zero synaptic weight. Conversely, in the crystalline phase, field confinement inside the resonator is weakened, coupling is reduced, and light predominantly propagates through the waveguide, corresponding to a high-transmission ("ON") state or high synaptic weight. These effects arise from simultaneous changes in both the real and imaginary components of GST's refractive index, effectively modulating optical phase and loss mechanisms.

By integrating GST with plasmonic structures, multiple advantages

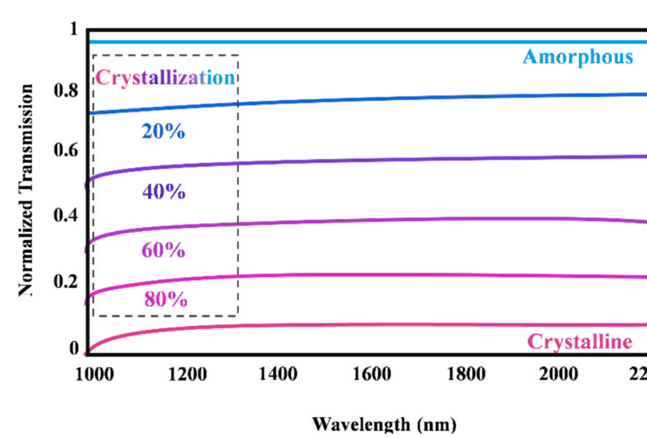

Fig. 4. Transmission spectra of the proposed structure at different crystallization levels of GST (10% to 80%), as well as the fully amorphous and fully crystalline states.

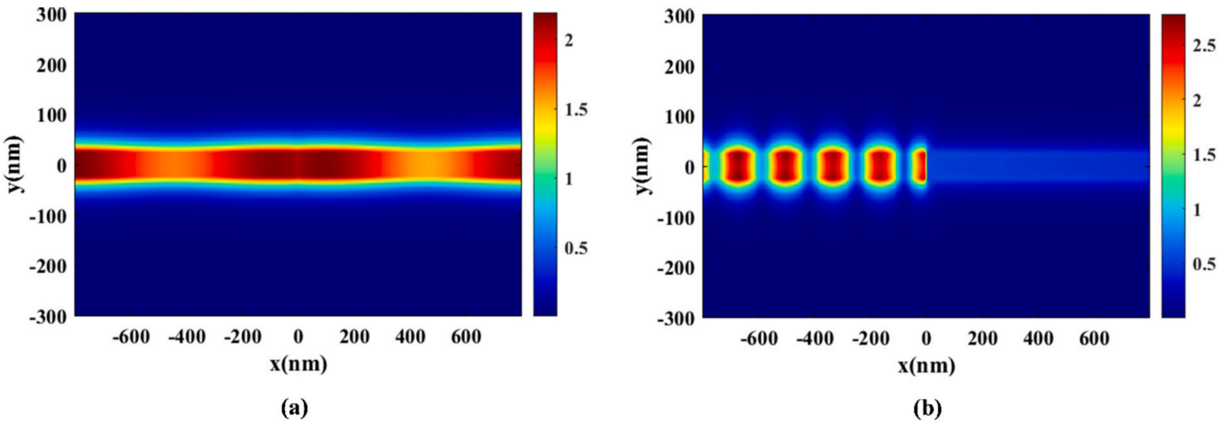

Fig. 5. Magnetic field distribution in the fully amorphous and fully crystalline phases corresponding to the structure shown in Fig. 3.

are realized, including intense field confinement, ultracompact device footprints, non-volatile optical modulation without holding power, and multilevel tunable synaptic weights. These properties enable the emulation of biological synaptic plasticity, where synaptic weights can be continuously tuned, facilitating the development of scalable neuromorphic photonic systems (Abdollahramezani et al., 2020 May 26; Prabhathan et al., 2023). Despite these benefits, challenges remain, such as ensuring thermal stability, repeatable switching, and structural robustness at the nanoscale, which require further investigation.

Building on this theoretical foundation, the following section presents the design of the proposed PCM-plasmonic nano-synapse (PPNS), detailing its structural configuration, operational principles, and anticipated neuromorphic performance.

3. Proposed PCM-Plasmonic Nano-Synapse (PPNS)

This section introduces the proposed plasmonic nano-synapse (PPNS) design based on the phase-change material (PCM) GST. The PPNS architecture consists of a nanoring resonator (NRR) coupled to two orthogonal waveguides: a horizontal control waveguide and a vertical data waveguide (Fig. 6). A nanometric triangular-shaped GST layer (20 × 55 × 80 nm^3) is strategically placed at the interface between the control waveguide and the NRR, serving as the active PCM modulating device.

Importantly, the PPNS leverages the intrinsic phase-change behavior of GST to emulate synaptic plasticity. In the amorphous phase, GST exhibits low absorption and a reduced refractive index, which facilitates strong coupling between the control waveguide and the NRR. This results in a resonant dip in the data waveguide transmission, corresponding to a low synaptic weight (OFF state). Conversely, in the crystalline phase, the higher refractive index and increased absorption weaken the coupling, allowing light to propagate largely unimpeded through the waveguide, corresponding to a high synaptic weight (ON state). This modulation directly mimics the dynamic adjustment of biological synaptic weights, enabling non-volatile, multi-level synaptic functionality in a compact plasmonic device.

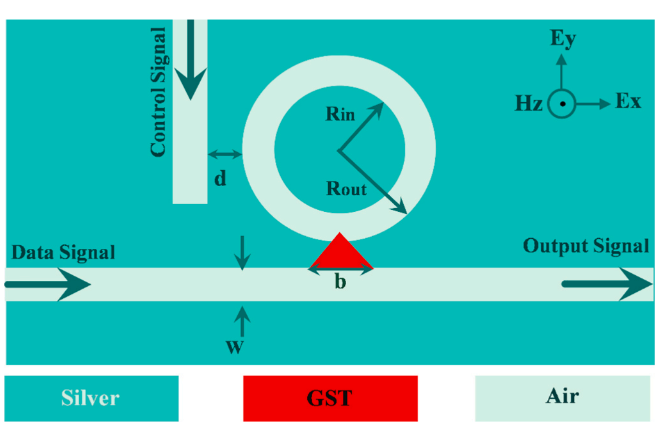

Fig. 6. Schematic of the GST–plasmonic nanoring resonator on a silver substrate in air, showing color-coded layers (green: air, white: silver, red: GST) and illustrating how GST phase transitions modulate plasmonic resonance and optical transmission. (For interpretation of the references to colour in this figure legend, the reader is referred to the web version of this article.)

The device is embedded in an air environment (refractive index n = 1) and supported on a silver substrate with a real refractive index of ~ 3 and a small imaginary component representing plasmonic loss, modeled using experimentally tabulated Johnson and Christy data. Silver is chosen for its low plasmonic absorption, which enhances resonator performance and reduces dissipative losses. In Fig. 6, air, silver, and GST are color-coded green, white, and red, respectively.

The reversible phase transition of GST between amorphous and crystalline states drastically modifies both its real (n) and imaginary (k) refractive index components (Wen et al., 2018 Mar 21). To quantify this, the effective optical constants of the coupled GST–waveguide–NRR system can be expressed as:

$$n_{eff} = n_a + X_c(n_c - n_a) \tag{2}$$

$$k_{eff} = k_a + X_c(k_c - k_a) \tag{3}$$

where n_a, k_a and n_c, k_c are the refractive indices of GST in amorphous and crystalline states, respectively, and X_c represents the crystallization fraction. This relationship provides a direct link between GST phase and effective optical properties, which modulate light–matter interactions within the NRR (Wu et al., 2022 Sep 29).

The effective optical constants in Equations (2) and (3) are calculated using an effective-medium approximation (EMA), where the optical response of partially crystallized GST is represented as a weighted combination of the amorphous and crystalline phases according to the crystallization fraction X_c (Ríos et al., 2015 Nov; Wuttig and Yamada, 2007 Nov; Rudé et al., 2013). This model assumes that the amorphous and crystalline domains are much smaller than the operating wavelength, allowing the GST layer to be treated as an optically homogeneous medium. Under this approximation, the effective refractive index components vary approximately linearly with the crystallization fraction, which has been widely adopted for modeling intermediate GST states in integrated photonic and plasmonic devices. Therefore, the proposed relations provide a physically valid and computationally efficient approach for analyzing resonance tuning, absorption modulation, and light–matter interaction in GST-integrated NRR structures.

In the crystalline phase, increased k_{eff} enhances plasmonic absorption and damps resonance intensity, resulting in strong transmission attenuation. In the amorphous phase, reduced absorption allows sustained resonance and higher transmission at the resonant wavelength.

The NRR geometry is parameterized by inner radius Rin = 250 nm, outer radius Rout = 300 nm, and inter-waveguide gap distance d = 15 nm, with waveguides width W = 50 nm. These parameters impact coupling efficiency, resonance linewidth, wavelength, and thereby the synaptic weight modulation capability. The resonance wavelength λ_res of the NRR is given by:

$$m\lambda_{res} = 2\pi R_{eff} n_{eff} \tag{4}$$

where m is the mode number, R_{eff} is the effective radius of the ring, and n_{eff} is the effective refractive index of the coupled ring-waveguide system (Pernice and Bhaskaran, 2012). GST phase changes, through n_{eff} and k_{eff}, shift λ_{res}, providing tunable resonance modulation.

The triangular GST shape induces local electric field enhancement ("tip enhancement") at corners, increasing light confinement, coupling efficiency between the control waveguide, GST, and NRR, and promoting rapid phase transitions, confirmed by FDTD simulations (Ríos et al., 2022 Oct 26). The energy coupling coefficients between the control waveguide, GST segment, and NRR, as well as between NRR and the data waveguide, depend on gap d, waveguide width W, and GST optical constants. GST phase modulates resonator loss: in the amorphous state, lower n_{eff} and k_{eff} reduce losses, enhancing resonance and transmission; in the crystalline state, increased k_{eff} suppresses resonance and decreases transmission. By modulating GST optically or electrically, the output data intensity can be tuned, implementing a programmable synaptic weight.

Synaptic contrast C is defined as:

$$C = \frac{T_{amorphouse} - T_{crystalline}}{Max(T_{amorphouse}, T_{crystalline})} \tag{5}$$

where $T_{amorphous}$ and $T_{crystalline}$ are the transmitted powers in the respective states. High contrast indicates clear differentiation between active and inactive synaptic states, enhancing accuracy and stability in neuromorphic photonic applications.

Fig. 7 illustrates the optical performance of the proposed structure: (a) Transmission ratio of the data waveguide for crystalline (blue) and amorphous (pink) GST. Normalized contrast (green) peaks at the resonance wavelength (2072 nm), demonstrating effective ON/OFF switching. (b) Transmission of the control waveguide (dB) for crystalline (blue) and amorphous (red) GST, showing strong attenuation (−30 to −40 dB), ensuring isolation of control from data paths.

The simulated electromagnetic field distribution (Fig. 8) confirms these transmission behaviors. In the amorphous phase (OFF state), coupling into the ring is efficient, producing a resonant dip (~0.02 transmission) and strong field localization. In the crystalline phase (ON state), weak coupling prevents resonance, and transmission remains high (~0.87), indicating a near-unity synaptic weight. Overall, this design demonstrates how GST's reversible phase change enables nonvolatile, tunable synaptic weights, directly emulating the plasticity observed in biological synapses. The mechanism modulating light transmission via phase-dependent coupling provides a robust and energy-efficient platform for neuromorphic photonic computing.

As a result, a pronounced resonance dip appears in the transmission spectrum, with the output dropping from nearly unity (outside resonance) to approximately 0.02 at the resonant wavelength. This suppression is clearly reflected in the electromagnetic field distribution, showing strong field confinement inside the nanoring and the surrounding GST region. In this amorphous phase, the resonator is active, enabling selective signal blocking at the target wavelength, effectively representing the "OFF" state or a near-zero synaptic weight, while transmission remains high at other wavelengths.

In contrast, in the crystalline phase, the increased real refractive index and reduced absorption of GST weaken the coupling between the waveguide and the nanoring. Consequently, light primarily propagates through the waveguide without significant interaction with the resonator. The ring resonance is inactive, and the transmission spectrum remains nearly flat and high (around 0.87). Field mapping confirms that the electromagnetic energy is concentrated along the waveguide, with minimal intensity inside the ring. This phase corresponds to the "ON" state or a high synaptic weight, indicating efficient signal transfer and an active synaptic channel.

Comparing the two GST phases demonstrates that the phase transition not only modulates coupling and resonance conditions but also directly determines the spatial field profile and the optical transmission at the output. The interplay of real and imaginary refractive index changes in GST simultaneously alters both optical phase and loss mechanisms. From a practical perspective, this mechanism enables nonvolatile, multi-level photonic synaptic switching, which is essential for scalable and energy-efficient neuromorphic photonic systems.

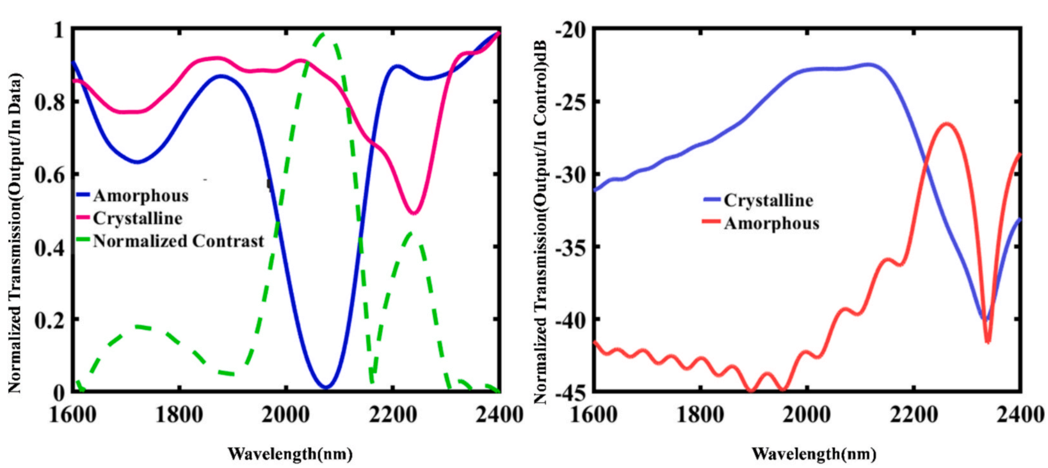

(a) (b)

Fig. 7. Illustrates the optical behavior of the proposed plasmonic nano-synapse under the two GST phase states: (a) Transmission ratio of the data waveguide as a function of wavelength for crystalline (blue curve) and amorphous (pink curve) phases. A pronounced transmission dip occurs at the resonance wavelength (2072 nm) in the crystalline phase due to strong absorption, while the amorphous phase maintains high, stable transmission. The normalized contrast curve (green) highlights the performance difference between the phases. (b) Control waveguide transmission (in dB) for crystalline (blue) and amorphous (red) phases, showing strong attenuation (−30 to −40 dB) indicating effective isolation of the control path from the data path. Minor variations due to GST refractive index changes exist but isolation performance is preserved. (For interpretation of the references to colour in this figure legend, the reader is referred to the web version of this article.)

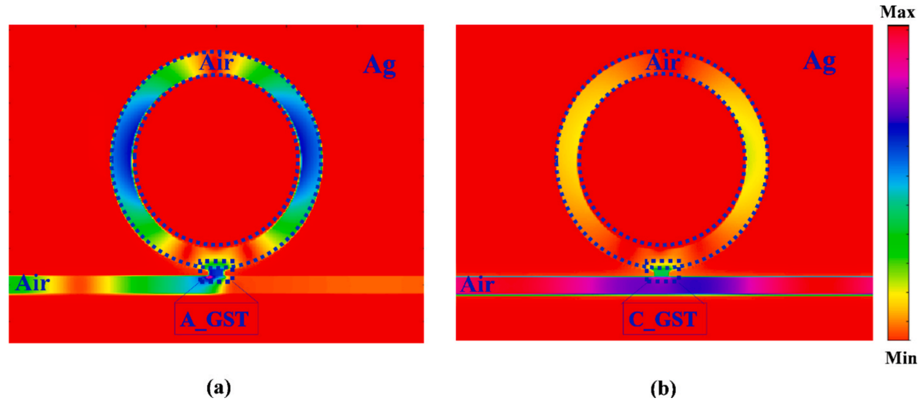

Fig. 8. Simulated electromagnetic field distribution and transmission behavior in the PPNS structure for two GST phases: In the amorphous phase, efficient coupling to the nano-ring activates resonance and reduces transmission at the target wavelength (OFF state). In the crystalline phase, the ring is inactive and light propagates directly through the waveguide (ON state).

Building on the structural design and optical functionality of the proposed PPNS, the next section focuses on switching performance modeling and thermal analysis. Understanding the thermal dynamics and heat transfer within the GST layer is crucial, as the reversible phase transitions underpin the synaptic weight modulation. Transient thermal simulations, combined with empirical data, allow precise estimation of temperature distribution, switching energy, and the impact of optical pulse parameters on device reliability and efficiency. This analysis provides the necessary framework to quantify and optimize the practical operation of the nanophotonic synapse, ensuring both energy-efficient and stable neuromorphic photonic behavior.

4. Switching performance modeling and thermal analysis of the proposed nanophotonic synapse based on GST

The switching operation in the proposed nanophotonic synapse structure is based on the phase-change material GST, whose atomic structure reversibly transitions between crystalline and amorphous states under controlled optical pulses. This phase change induces significant variations in the optical and thermal properties of the GST layer and forms the foundation for synaptic weight modulation (Wuttig and Yamada, 2007 Nov; Zhang et al., 2019; Loke et al., 2012; Zeng et al., 2024 Dec 23). To precisely understand the heat transfer mechanisms and temperature distribution, transient thermal simulations were conducted considering the actual dimensions of the GST layer, $20 \times 55 \times 80$ nm^3.

As illustrated in Fig. 9, the temperature profiles of the GST layer under two critical operating conditions are presented. In the crystalline state (SET) with a long pulse at 5 mW power (Fig. 9a), the generated heat is distributed more uniformly throughout the GST volume, resulting in a gradual and extensive temperature rise. These uniform thermal conditions promote homogeneous crystallization and the recovery of the original optical properties (Simpson et al., 2010 Feb 10). In contrast, in the amorphous state (RESET) with a short pulse at 20 mW power (Fig. 9b), a severe temperature concentration and energy absorption occur at the center of the GST layer, coinciding with the region of maximum electric field intensity. This localized energy accumulation increases the local energy density, raising the temperature close to the material's melting point, thereby enabling a rapid and complete phase transition to the amorphous state (Kiselev et al., 2022 Mar).

These fundamental differences in temperature distribution form the basis for functional variations in the synapse operation and directly demonstrate the critical influence of optical pulse characteristics on the phase transition process.

These precise thermal simulations effectively highlight the significant impact of pulse parameters on the phase-transition mechanism and consequently on the device performance.

To address the theoretical aspects, a Multiphysics model incorporating transient heat conduction and localized optical absorption derived from electromagnetic simulations is expressed as (Zhang et al., 2019; Wright et al., 2019):

$$\rho(T)C_p(T)\frac{\partial T(r,t)}{\partial t} = \nabla.[\kappa_{th}(T)\nabla T(r,t)] + Q_{abs}(r,t) \quad (4)$$

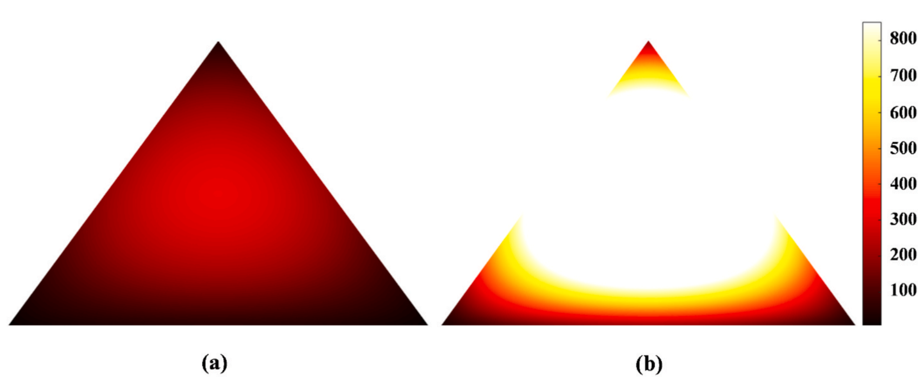

Fig. 9. Transient thermal analysis of the GST-based plasmonic nano-ring synapse with actual GST dimensions of 20 × 55 × 80 nm320 × 55 × 80 nm3. Temperature distribution maps under two critical operational states: (a) amorphous (RESET) phase induced by a short optical pulse at 20 mW, showing localized high temperature concentration at the nano-ring center leading to melting and rapid phase transition; (b) crystalline (SET) phase with a longer optical pulse at 5 mW, resulting in more uniform heating and gradual temperature rise, favorable for homogeneous crystallization. These thermal profiles underscore the essential role of optical pulse parameters in precise switching control and stable synaptic operation.

$$Q_{abs}(r,t) = \frac{1}{2}\omega\varepsilon_0\varepsilon^{''}(T,\varphi)|E(r,t)|^2 \quad (5)$$

Where $\varepsilon''(T,\phi)$ is the temperature- and crystallinity-dependent imaginary part of the permittivity and $|E(r,t)|^2$ denotes the local electric field intensity (Simpson et al., 2011). The phase transition dynamics are modeled using the Johnson-Mehl-Avrami-Kolmogorov (JMAK) kinetics:

$$\varphi(t) = 1 - exp(-K(T)t^n) \quad (6)$$

where $\phi(t)$ represents the crystallization fraction, K(T) is the temperature-dependent rate constant, and n is the crystal growth exponent.

Due to the complexity and inherent discontinuities in thermal models and energy transfer within this structure, direct estimation of switching energy solely through Multiphysics simulation is challenging (Hosseini et al., 2014). Therefore, the switching energy is estimated by combining high-fidelity thermal simulations of the temperature distribution using the actual GST volume ($20 \times 55 \times 80\ nm^3$) and empirical data from reported experimental values in well-established ISI-indexed literature (Zhang et al., 2020).

The switching energy is approximated to lie within the range of 4 to 8 picojoules, consistent with the reported findings in the literature. This estimated range reasonably accounts for thermal losses, nonuniform absorption, thermal boundary resistance, and other inevitable non-idealities present in real systems. For a first-order energy estimate, the classical heat capacity relation is used:

$$E_{switch} = V_{GST} \times \rho \times C_p \times \Delta T \quad (7)$$

Where $\rho \approx 6150\ kg/m^3$ is the density of GST, $V_{GST} = 20 \times 55 \times 80\ nm^3 = 8.8 \times 10-^{23}\ m^3$ is the actual GST volume, $Cp \approx 200\ J/(kg\cdot K)$ is the specific heat capacity, $\Delta T \approx 800$ Kis the temperature change required for Reset (Abou El Kheir et al., 2024).

Numerical substitution provides an initial energy estimate of approximately 0.065 pJ. However, as reported in previous studies, the actual switching energy is typically an order of magnitude higher due to thermal dissipation, nonuniform heating, and other practical device limitations. By applying an empirical correction factor, an effective switching energy range of 4 to 8 pJ (adopting 5 pJ for this work) is justified and aligns with experimental observations (Zheng et al., 2018 May 17). Although numerical models solving coupled thermal and optical equations can offer higher accuracy, they require precise parameters and boundary conditions that are often limited in theoretical studies. Therefore, in this work, thermal simulations were conducted reflecting the exact dimensions and operating conditions of the GST layer, switching power and energy estimates were grounded on existing experimental evidence from recognized journals to ensure reliability, and advanced analytical models were referenced mainly to provide a theoretical framework and enable comparison with the scientific literature (Zhou et al., 2021; Wang et al., 2022 Mar 1; Pobegen et al., 2016).

Thermal analysis, Multiphysics modeling, and empirical energy estimates collectively demonstrate that the proposed GST-based nanophotonic synapse can achieve stable, rapid switching with optimized energy consumption in the range of 4 to 8 picojoules (taken as 5 pJ here). Careful control of optical pulse parameters, including power and duration, optimizes thermal distribution and phase transition dynamics, leading to improved device performance and reduced energy usage (Johnson et al., 1972). These characteristics make the proposed nanophotonic synapse an excellent candidate for efficient, multi-level learning neuromorphic photonic systems characterized by low power consumption and high scalability.

The precise control of phase transitions in GST, established through thermal simulations and switching performance modeling, directly informs the spectral behavior of the proposed nanophotonic synapse. The crystallization fraction and localized temperature distribution not only determine the ON/OFF synaptic states but also modulate the effective refractive index and absorption profile of the GST layer. Consequently, these thermal and material dynamics play a critical role in shaping the resonance characteristics, transmission spectra, and synaptic weight tunability. In the following section, we explore spectral engineering and transmission control, linking phase-change dynamics to resonance optimization and multilevel synaptic modulation in GST-based ring resonator nano-synapses.

5. Spectral engineering and transmission control in GST-Based ring resonator Nano-Synapses

Precise control of spectral response and transmission dynamics in plasmonic nano-synapse architectures is essential for optimizing neuromorphic photonic systems. In GST-integrated nano-ring resonators, both the geometric design of the resonator and the engineered geometry of the GST phase-change segment play direct and synergistic roles in spectral tunability, resonance selectivity, and switching contrast (Wuttig and Yamada, 2007 Nov). By adjusting the inner and outer radii of the resonator, it is possible to modulate the resonance wavelength and linewidth, enabling customizable multi-wavelength operation and improved selectivity. Simultaneously, tailored GST geometry—particularly in the form of a triangular patch—amplifies field localization at critical regions, influencing phase transition thresholds and maximizing transmission contrast between amorphous and crystalline states. These approaches pave the way for achieving high-performance, programmable, and energy-efficient synaptic modulation for advanced photonic computing applications (Ríos et al., 2015 Nov).

5.1. Spectral tunability through inner and outer radius engineering in the ring resonator

Following the confirmation of the GST phase-state impact on the resonant and transmission characteristics of the device, one of the key advantages of ring-based architectures lies in their inherent capability to tailor optical properties via precise geometric modifications. Here, we investigate the influence of independently varying the inner and outer radii of the proposed resonator on its spectral tunability while maintaining robust switching performance.

Fig. 10a depicts the variation of transmission contrast as a function of the operating wavelength and the outer radius R_{out} with the inner radius kept constant. An increase in R_{out} induces a redshift in the resonance wavelength, originating from the elongation of the effective optical path length, which in turn lowers the resonance frequency. The high-contrast region (bright yellow) maintains a narrow spectral bandwidth and sharp roll-off, indicative of high spectral selectivity and operational stability even under dimensional perturbations. Notably, the peak contrast consistently exceeds 0.8, confirming the effectiveness of outer-radius variation for coarse spectral tuning.

Fig. 10b examines the effect of inner radius variation R_{in} while holding R_{out} constant. Similar to the outer-radius case, increasing Rin produces a redshift in the resonance; however, the magnitude of the shift is more substantial due to the stronger influence of the inner boundary on optical mode confinement and the effective refractive index within the ring. Across the full range of inner-radius variations, the maximum contrast remains stable between 0.75 and 0.85, demonstrating the preservation of high switching quality.

These results clearly indicate that independent control over the inner and outer radii enables both coarse and fine spectral tuning without compromising transmission contrast. This geometric degree of freedom renders the proposed structure a strong candidate for neuromorphic photonic systems, where precise wavelength alignment is vital for implementing and dynamically programming synaptic weights in optical neural networks.

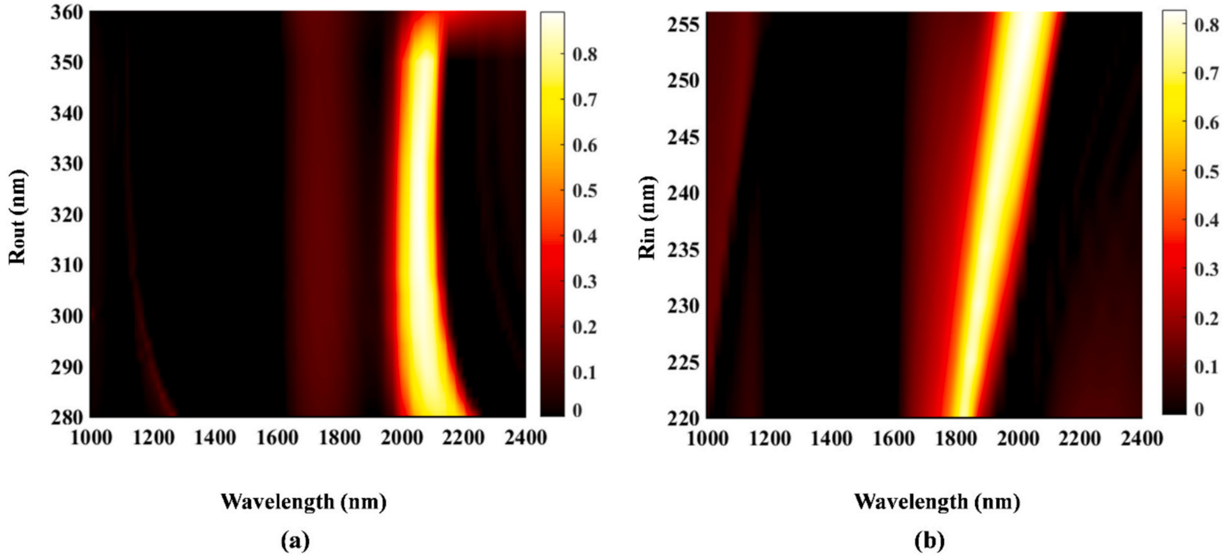

Fig. 10. Transmission contrast of the nano-ring synaptic structure as a function of operating wavelength and (a) outer ring radius and (b) inner ring radius. In both cases, increasing the radius shifts the resonance to longer wavelengths, while the high-contrast region remains spectrally narrow and stable. This dimensional tunability enables both coarse and fine resonance tuning without significant loss in switching performance.

5.2. Impact of GST triangle geometry on spectral tunability and transmission contrast

This section investigates the influence of geometrical modifications in the triangular GST region on the spectral response and transmission contrast of the proposed device. The studied parameters include the triangle height h_{GST} and the triangle base length b_{GST}, as illustrated in Fig. 11a and b, respectively.

In Fig. 11a, the transmission contrast is plotted as a function of wavelength and h_{GST} . As the height increases, the GST volume intersecting the optical path grows, which modifies the effective refractive index and increases the optical path length. This results in a redshift of the resonance wavelength. Furthermore, the high-contrast region remains spectrally narrow and stable for medium-to-large heights, indicating robust switching performance under height variations.

In Fig. 11b, the effect of b_{GST} on the spectral behavior is examined while keeping other parameters fixed. Increasing the base length enlarges the effective interaction area between the guided mode and the GST material, altering the modal field distribution and the coupled plasmonic modes. Similar to height variation, this produces a redshift in the resonance wavelength. However, the changes in peak position and contrast profile exhibit slight differences due to the distinct impact on the coupling region. Notably, the maximum contrast remains within the 0.75–0.85 range over the entire base variation, demonstrating that this parameter also enables wavelength tuning without degrading the switching performance.

Overall, the results in Fig. 11 confirm that geometrical tailoring of the GST region, via both height and base length, provides an effective means for spectral tuning of the device without significant contrast deterioration. This tunability is particularly advantageous in

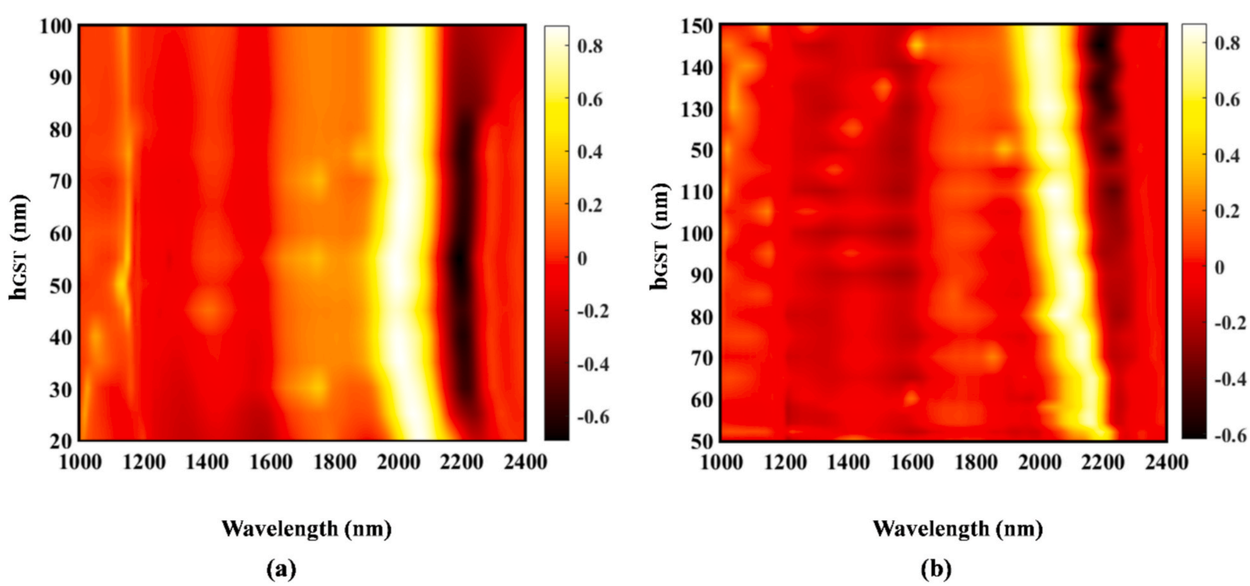

Fig. 11. Impact of geometric variations in the triangular GST region, including the triangle height and base length, on the spectral response and transmission contrast of the nano-ring synaptic structure. Increasing either parameter shifts the resonance wavelength toward longer wavelengths, while the high-contrast region remains narrow and stable. These results demonstrate that precise wavelength tuning can be achieved through GST geometry modification without noticeable degradation in switching performance, highlighting its importance for neuromorphic photonic applications and the implementation of optical synaptic weights.

neuromorphic photonic applications, where precise wavelength alignment is essential for implementing and dynamically adjusting synaptic weights in optical neural networks.

The spectral engineering strategies and transmission control methods discussed in the previous section lay the groundwork for advanced synaptic functionalities. By precisely tailoring the resonator geometry and the GST triangular segment, it is possible to achieve high-contrast, tunable transmission that can differentiate multiple synaptic states. Building on this capability, the next section introduces a novel framework for bipolar synaptic weight realization, where both positive and negative transmission contrasts are harnessed to emulate excitatory and inhibitory synaptic behaviors in a single GST–plasmonic structure. This approach leverages the engineered spectral response to implement versatile, multilevel synaptic weight modulation for neuromorphic photonic systems.

6. A novel framework for bipolar synaptic weight realization via Positive and negative transmission contrast in GST–Plasmonic structures

Based on an extensive survey of the existing literature, the concept of positive and negative transmission contrast has not yet been independently identified, systematically analyzed, or exploited as a fundamental physical mechanism for realizing bipolar synaptic behavior in plasmonic synapses incorporating phase-change materials such as GST (Wu et al., 2022 Aug 2; He et al., 2025 Jul). In this work, we introduce, for the first time, a rigorous and unified framework in which bipolar synaptic weights emerge naturally from the spectral sign reversal of the transmission contrast between the amorphous and crystalline phases of GST.

This approach establishes a direct physical bridge between the wavelength-dependent resonance behavior of plasmonic nanostructures and synaptic weight polarity in neuromorphic photonic systems (Abdollahramezani et al., 2022; Oh et al., 2019; Farmakidis et al., 2019). Beyond its conceptual novelty, this framework provides a practical route toward implementing both excitatory and inhibitory learning functionalities within a single, compact optical synapse, eliminating the need for duplicated hardware elements or auxiliary control circuitry. As a result, the proposed scheme significantly advances the scalability, efficiency, and functional density of photonics-based spiking neural networks and contributes to the broader development of intelligent and adaptive photonic systems (Chen et al., 2022; Go et al., 2021; Jankovic and Cselyuszka, 2018; Li et al., 2023; Zhang et al., 2022).

6.1. *Geometric and spectral control of bipolar transmission contrast in GST–Plasmonic ring resonators for synaptic STDP learning*

resonator reveal that the transmission contrast spectrum intrinsically exhibits both positive and negative regions. At certain wavelengths, transmission in the amorphous phase exceeds that in the crystalline phase, whereas at other wavelengths, the opposite behavior occurs. Fig. 12 presents a two-dimensional map of the transmission contrast for a fixed resonator geometry and varying GST crystallization degrees, clearly delineating two distinct operational regions: a positive region corresponding to excitatory synaptic behavior (LTP) and a negative region corresponding to inhibitory synaptic behavior (LTD) (Shastri et al., 2021 Feb; Ahmadi et al., 2024 Dec 30). These results indicate that the synaptic polarity is primarily determined by the operating wavelength, while varying the crystallization degree enables the implementation of multilevel synaptic weights without altering the bipolar nature (Shastri et al., 2021 Feb).

Fig. 13(a) highlights the dominant role of the ring inner radius (R_{in}) in determining the spectral positions of these bipolar regions. Increasing R_{in} results in a systematic redshift of the resonances and a corresponding shift in the zero-crossing wavelengths, which define the boundary between LTP and LTD regions. In contrast, Fig. 13(b) illustrates the effect of the triangular GST height on the amplitude of transmission contrast;

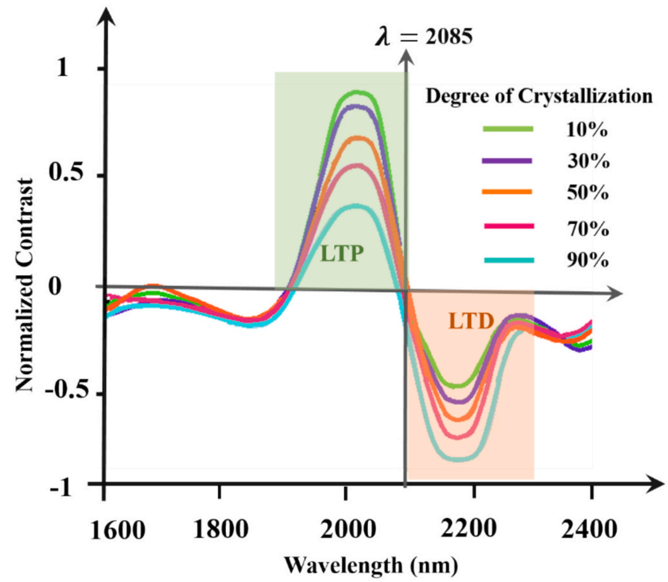

Fig. 12. Two-dimensional transmission contrast spectra for different degrees of GST crystallization (10%–90%) at fixed resonator geometry. The shaded regions indicate excitatory (LTP) and inhibitory (LTD) operational wavelengths. Increasing crystallization level enables multi-level synaptic weighting by modulating contrast magnitude while preserving bipolar polarity.

increasing the GST height enhances the absolute contrast and improves synaptic state discrimination, while the spectral positions of the bipolar boundaries remain largely controlled by R_{in}.

By simultaneously tuning R_{in} and the GST height, the proposed structure enables independent control of both the spectral position and amplitude of the bipolar transmission contrast, providing a robust physical basis for implementing excitatory and inhibitory weight modulation in a compact plasmonic element. This feature is critically important for analog neuromorphic applications and the realization of STDP-based learning in optical synapses (Shastri et al., 2021 Feb; Ahmadi et al., 2024 Dec 30).

6.2. *Implementation of STDP learning via spectral and pulsed control in the proposed GST–Plasmonic Synapse-Based optical spiking neural network*

As described in Section 2.1, spike-timing-dependent plasticity (STDP) is a fundamental learning rule in spiking neural networks (SNNs), playing a central role in memory formation and information processing. In this mechanism, the sign and magnitude of synaptic weight changes are determined by the temporal difference between the arrival of pre- and post-synaptic spikes: if the pre-synaptic spike arrives earlier, the synaptic weight increases (positive/excitatory; long-term potentiation, LTP); if it arrives later, the weight decreases (negative/inhibitory; long-term depression, LTD).

Hardware implementation of this mechanism in conventional electronic or photonic architectures is challenging due to the need for precise timing control and often relies on multiple physical units or centralized controllers. This challenge is further exacerbated in fully optical, ultrafast systems, where events occur on picosecond to nanosecond timescales. Moreover, in standard approaches, achieving simultaneous bipolar excitatory/inhibitory weighting typically requires two separate structures, resulting in increased hardware volume and energy consumption.

In the proposed architecture, for the first time, the classical temporal axis in STDP is replaced by the spectral (wavelength) axis. This approach enables the realization of both excitatory (positive) and inhibitory (negative) synaptic weights within a single GST–plasmonic ring

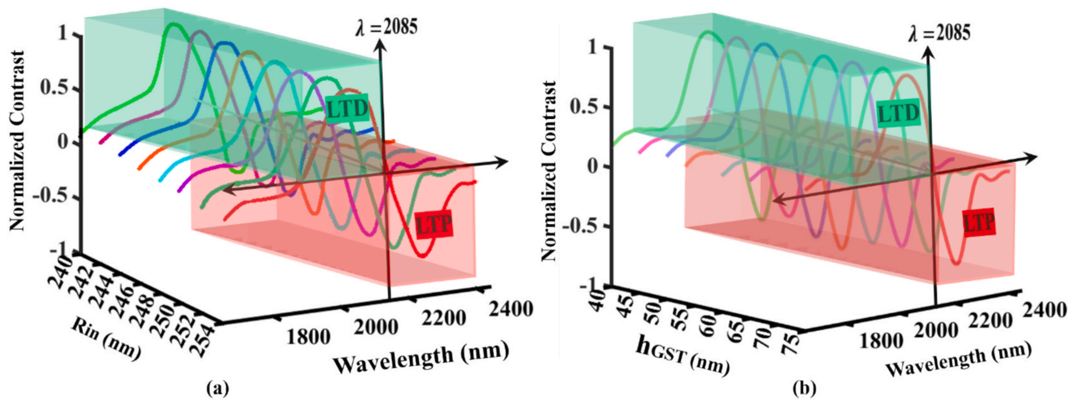

Fig. 13. Revised transmission contrast spectra (ΔT) of the GST–plasmonic ring resonator illustrating bipolar synaptic operation. (a) Effect of inner ring radius (Rin) on the spectral position of excitatory ($\Delta T > 0$, LTP) and inhibitory ($\Delta T < 0$, LTD) regions. Increasing Rin induces a red shift of the resonance peaks and moves the zero-crossing wavelength that separates LTP and LTD regimes.(b) Effect of the triangular GST height on the magnitude of ΔT. While larger GST height enhances the contrast amplitude, the spectral boundary between excitatory and inhibitory regions remains primarily governed by Rin. The shaded regions explicitly indicate LTP and LTD operational domains. (For interpretation of the references to colour in this figure legend, the reader is referred to the web version of this article.)

resonator, without requiring additional elements or structures. By selecting the operational wavelength, the GST region undergoes either amorphization (LTP, excitatory) or crystallization (LTD, inhibitory), dynamically setting the synaptic weight according to the STDP rule.

The pre-synaptic input pulse, injected through the primary waveguide, represents the pre-synaptic neural spike. The post-synaptic feedback pulse, generated by the output neuron, is directed into the synapse's control waveguide. When these two pulses overlap in the GST region at a selected wavelength, the accumulated energy induces a phase transition between amorphous and crystalline states. At wavelength λ_{LTP}, if the total energy exceeds the melting threshold, optical transmission increases, corresponding to LTP (excitatory weight). At wavelength λ_{LTD}, sufficient energy leads to crystallization, corresponding to LTD (inhibitory weight). This mechanism ensures that the GST phase directly modulates the synapse's transmission coefficient and its connection weight.

Fig. 14 schematically illustrates the network architecture of an optical spiking neural network, consisting of one output neuron and multiple input neurons. In this design, each synapse is composed of three main components: an input waveguide that receives the pre-synaptic neural signal, a control waveguide that carries the post-synaptic feedback signal, and a GST–plasmonic ring resonator serving as the active region whose phase change dictates the synaptic weight. The input signal is directly injected into the resonator, while the feedback signal from the network output is routed back into the control waveguide, regulating the weight update in accordance with the STDP rule.

Fig. 15 illustrates the temporal and energy profiles of the two pulse types applied to the synapse. The input pulse is an optical signal injected through the input waveguide, emulating the pre-synaptic neural spike. Its energy and duration are tuned so that it cannot independently trigger a full phase transition, but when combined with the feedback pulse, it enables synaptic weight adaptation. The control feedback pulse, delivered after post-synaptic neuron activation, is applied back to the synaptic control waveguide via the feedback pathway. The temporal and energetic overlap of the two pulses in the GST region governs the outcome of STDP learning, either potentiation or depression. This figure

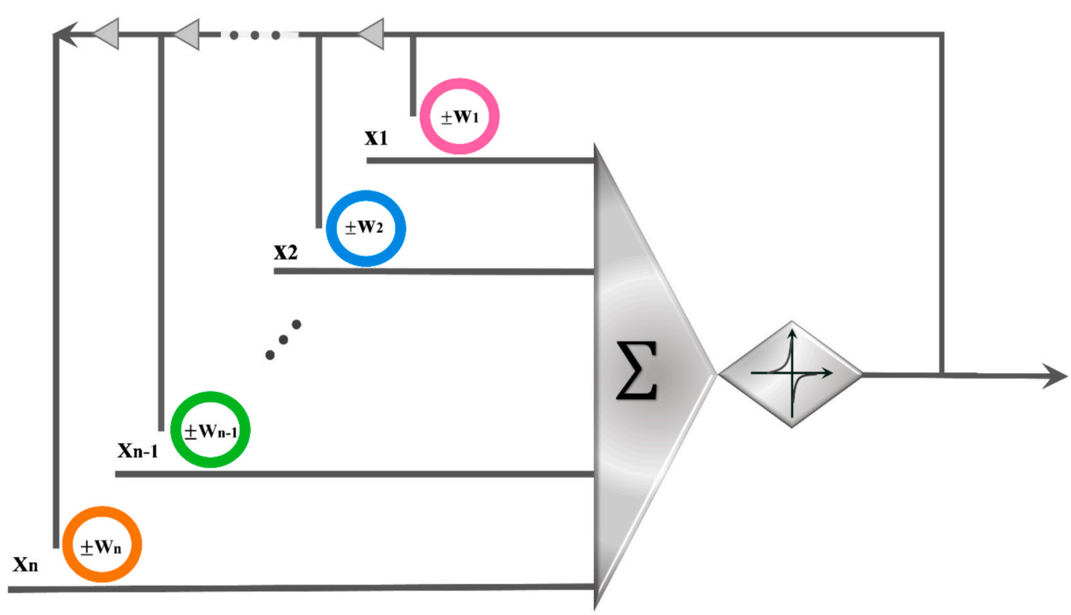

Fig. 14. Each synapse consists of an input waveguide and a control feedback waveguide coupled to a GST–plasmonic ring resonator. The phase-change state of GST, controlled by the timing and spectral overlap of input and feedback pulses, dynamically sets the synaptic weight according to the STDP rule. This figure shows the proposed structure of our work, highlighting the integration of excitatory and inhibitory weights within a single synapse.

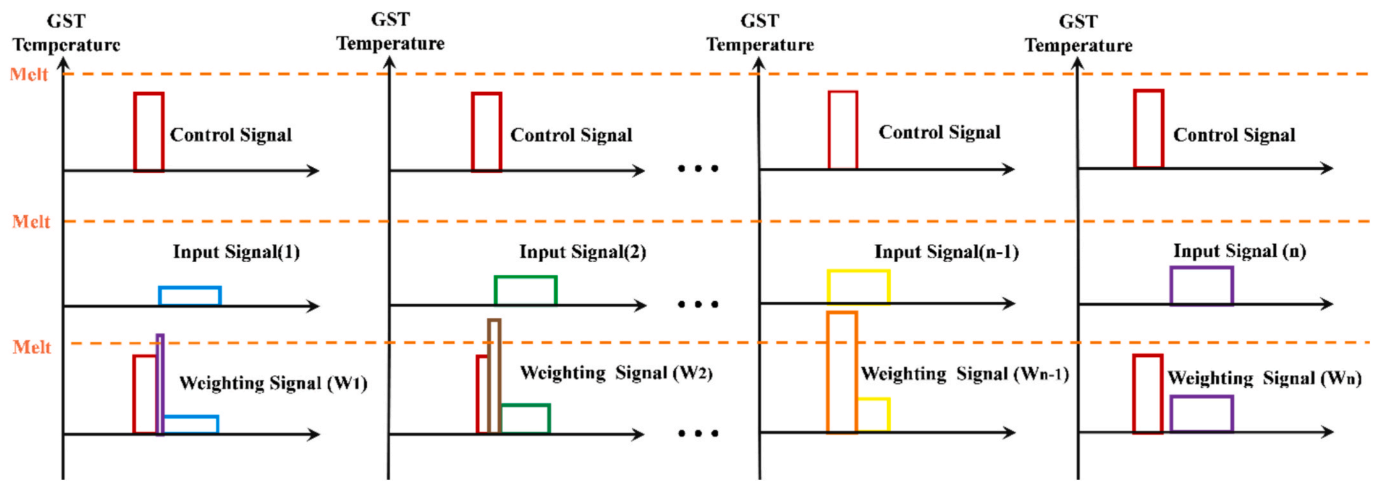

Fig. 15. Temporal and energy profiles of input and feedback pulses applied to the GST region of each synapse. The relative arrival time and cumulative energy of these pulses determine whether the synapse undergoes potentiation (amorphization, excitatory weight) or depression (crystallization, inhibitory weight), based on the chosen operational wavelength and pulse overlap. This figure demonstrates the simultaneous implementation of bipolar synaptic weights within one device.

clearly demonstrates the realization of bipolar synaptic weights within a single device.

The advantages of this design are that both excitatory and inhibitory synaptic weights are implemented within a single element, which

Table 1
Comparative overview of photonic and plasmonic structures based on phase-change materials (PCM) in recent years, highlighting structure type, configuration mechanism, PCM, normalized optical contrast, device footprint, PCM volume, switching energy, and supported synaptic weight polarity. The present work demonstrates an ultra-compact plasmonic switch with high contrast, minimal footprint, and low switching energy, enabling both positive and negative synaptic weights.

Ref.	Year	Structure type	Configuration Mechanism	PCM	Normalized Contrast	Footprint (μm^2)	Volume of PCM (µm3)	Switching Energy (pJ)	Bipolar Weight (±)
(Ríos et al., 2015 Nov)	2015	Silicon	All-Optical	GST	21%	1	0.01	430	Positive
(Go et al., 2021)	2017	Silicon	All-Optical	GST	14%	900	19.6	20	Positive
(Stegmaier et al., 2017 Jan)	2017	Silicon	All-Optical	GST	74.30%	3600	0.009	190	Positive
(Cheng et al., 2017 Sep 27)	2017	Silicon	All-Optical	GST	95%	506	0.008	216–404	Positive
(Hosseini et al., 2014)	2018	Silicon	All-Optical	GST	99.90%	3600	——————	620	Positive
(He et al., 2025 Jul)	2019	Plasmonic	Opto-Electric	GST	29.40%	——	0.0018	16	Positive
(Xu et al., 2019 Jan 7)	2019	Silicon	All-Optical	GST	90.00%	225	0.048	——	Positive
(Feldmann et al., 2019 May 9)	2019	Silicon	All-Optical	GST	87.40%	183,600	0.36	430/710	Positive
(Wu et al., 2018 Dec 19)	2019	Silicon	All-Optical	GST	84%	625	0.019	250	Positive
(Zhang et al., 2019 Sep 30)	2019	Silicon	Opto-Electric	GSST	99.90%	224,200	0.008	——	Positive/ Negative
(Zhang et al., 2020 Jun 16)	2020	Silicon	All-Optical	GST	99%	225	0.032	——	Positive
(Farmakidis et al., 2022 Jul)	2022	Plasmonic	Opto-Electric	GST	90%	———	0.01	4000	Positive
(Feldmann et al., 2017 Nov 2)	2022	Silicon	Opto-Electric	GST	19.90%	250	0.008	380,000	Positive
(Ríos et al., 2015 Nov)	2022	Silicon	Opto-Electric	Sb2Se3	90%	1000	0.36	176,000	Positive/ Negative
(Li et al., 2022 Jul)	2022	Silicon	All-Optical	In2Se3	30.80%	425	0.019	400/700	Positive
(Song et al., 2022 Aug 3)	2022	Silicon	Opto-Electric	Sb2S3	99.90%	124.46	0.032	9590	Positive
(Brückerhoff-Plückelmann et al., 2023 Oct)	2023	Silicon	Opto-Electric	GST	67%	7590	0.017	——	Positive
(Nohoji et al., 2024 May)	2024	Photonic crystal	All-Optical	GST	84.50%	2916	3.22	——	Positive
(Chen et al., 2024)	2024	Silicon	Opto-Electric	GST	99.50%	51.8	0.054	——	Positive
(Ghosh and Dhawan, 2022 Nov 1)	2024	Silicon	All-Optical	Sb2Se3	99.60%	132	0.24	21,000	Positive
(Sharifipour et al., 2025 Jun)	2025	Plasmonic	All-Optical	GST	97.70%	0.036	0.000078	8	Positive
(Sharifipour et al., 2025 Aug 11)	2025	Plasmonic	All-Optical	GST	98.00%	0.031	0.000078	7	Positive
(Sharifipour et al., 2025 May 31)	2025	Plasmonic	All-Optical	GST	77.90%	0.14	0.000072	8	Positive
This Work	2025	Plasmonic	All-Optical	GST	99%	0.09	0.000044	5	Positive/ Negative

significantly reduces the physical footprint and optimizes the overall power consumption of the system. Synaptic weight updates occur on extremely short timescales, from picoseconds to nanoseconds, utilizing the inherently parallel processing nature of photonic systems, and all learning processes are governed by the natural overlap of input and feedback pulses, eliminating the need for a central controller.

7. Comparative performance analysis

Based on the comparative presented in Table 1, the proposed design in this study demonstrates superior and innovative performance across multiple key aspects relative to previous works. Employing a plasmonic all-optical configuration (PPNS) integrated with the phase-change material GST, the device achieves a remarkably high normalized contrast of 99%, positioning it among the highest values reported in the literature. Such a high contrast evidences precise and high-quality optical switching dynamics, crucial for robust neuromorphic photonic functionalities.

Another outstanding advantage of this design is its exceptionally compact footprint of only 0.09 μm^2, which is significantly smaller than commonly reported silicon-based micro-ring resonator (MRR) or waveguide devices, whose footprints typically range from several hundreds to thousands of square micrometers. This extreme footprint reduction directly enables ultra-high integration density and scalability for practical on-chip photonic neuromorphic applications.

The volume of the phase-change material GST is also greatly minimized to approximately 0.000044 μm^3, which represents a substantial reduction compared to volumes documented in similar nanoscale devices. This volume optimization critically contributes to energy efficiency; indeed, switching energy has been estimated through five independent methods in this work, consistently indicating low energy consumption on the order of a few picojoules. This value is markedly lower than most previously reported devices, demonstrating significant progress in energy-efficient neuromorphic operation.

One of the most distinguishing features of the proposed synapse is its ability to realize bipolar synaptic weights (both positive and negative) within a single device structure. This capability relies on an intelligent resonance wavelength shift mechanism in the plasmonic nano-ring, whereas prior studies typically required two separate synaptic elements to achieve bipolar weighting. Such an integrated approach reduces hardware complexity, lowers power consumption, and enhances device density and scalability.

Structurally, the design benefits from strong localized plasmonic electromagnetic fields generated by the silver underlayer and air cladding, which enable rapid and energy-efficient phase switching of GST. Compared to other plasmonic devices that exhibit optical contrasts ranging from 29% to 90%, with larger footprints and higher switching energies, the present work uniquely integrates the following: near-ideal optical contrast (~99%), an ultra-compact footprint (<0.1 μm^2), a minimally sized GST volume with highly optimized switching energy in the picojoule range, and the simultaneous realization of both positive and negative synaptic weights within a single compact element.

Together, these advancements establish a new state-of-the-art benchmark in the field of nanoscale photonic synapses and pave the way for next-generation neuromorphic photonic systems, characterized by low power consumption, high compactness, and multifunctional synaptic learning capabilities.

8. Fabrication feasibility

The proposed GST–silver plasmonic nanophotonic synapse is not only theoretically efficient but also fully compatible with current state–of–the–art nanofabrication infrastructures. Fig. 16 illustrates the conceptual three–dimensional fabrication flow. The entire process leverages fabrication steps that are widely employed in both academic nanophotonics laboratories and large–scale semiconductor manufacturing, underscoring its practicality and industrial relevance.

The fabrication begins with deposition of a silver (Ag) plasmonic underlayer on a suitable substrate to form the bottom metal for the metal–insulator–metal (MIM) configuration. Low–loss Ag films can be achieved using thermal evaporation or magnetron sputtering, followed by standard lift–off techniques to ensure uniform thickness and smooth surfaces. The use of silver surrounded by a low–index cladding such as air significantly enhances the localized electromagnetic field and optimizes light–matter interaction, as extensively discussed in recent plasmonics literature (Nur-E-Alam et al., 2021 Jul 22).

Plasmonic waveguides and nanoring resonators are then patterned using electron–beam lithography (EBL) and focused ion beam (FIB) milling. These techniques routinely achieve sub–10 nm resolution and allow reproducible fabrication of nanoscale features such as the 50 nm triangular GST region and the 50 nm air–clad waveguide (Basu et al., 2025 Mar 26; Utke et al., 2012 May 1). After the resist is removed, the resulting structure forms a free–standing air–clad plasmonic resonator.

Selective deposition of the $Ge_2Sb_2Te_5$ (GST) layer onto the nanoring is performed through a second lithography step combined with lift–off. Numerous experimental studies have successfully demonstrated

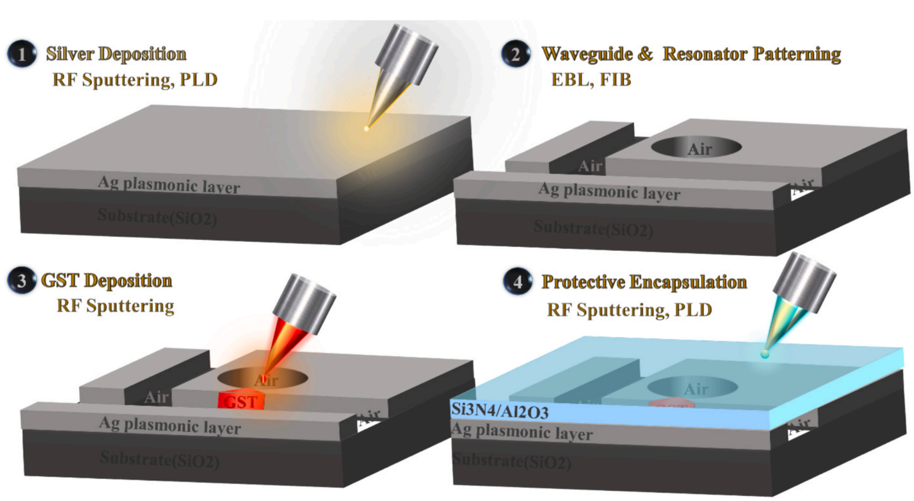

Fig. 16. Fabrication flow of the GST–silver plasmonic nanoring resonator. The process includes Ag deposition, patterning of waveguides and the nanoring via EBL/FIB, air-clad structure formation, selective GST deposition through lift-off, and optional protective ALD coatings (Si_3N_4 or Al_2O_3) to ensure device stability and compatibility with non-volatile optical switching.

high–quality GST deposition—down to thicknesses below 100 nm and even onto complex metallic geometries—using RF magnetron sputtering and pulsed laser deposition (PLD) (Boschker and Calarco, 2017 May 4; Sreekanth et al., 2019; Simandan et al., 2021 Jun 30; Parra et al., 2022 Jun 13). These deposition techniques ensure precise control over GST thickness, stoichiometry, and phase transition behavior, which is essential for reliable switching performance.

The reversible phase transition between amorphous and crystalline states enables non–volatile, reconfigurable, and low–energy optical behavior. After fabrication, optical characterization methods such as transmission spectroscopy, NSOM, and pump–probe measurements can accurately assess the spectral response and phase–change dynamics of GST–based devices (Shalini, 2013). GST's thermal stability at nanoscale dimensions has also been validated extensively, supporting robust and repeatable device operation.To improve environmental durability, thin conformal encapsulation layers—such as Si_3N_4 or Al_2O_3—can be deposited using atomic layer deposition (ALD). These coatings protect both GST and Ag from oxidation and surface degradation while preserving the device's plasmonic properties (Lee et al., 2023 Mar 6; Gao et al., 2020 Jan).

Industrial and practical relevance. Beyond laboratory demonstrations, the feasibility of our structure is strongly reinforced by the widespread industrial use of GST in commercial phase–change memory (PCM) products from Intel and Samsung, where GST is deposited, cycled, and encapsulated at scale with extremely high reliability. These manufacturing processes directly mirror the material and thermal–cycling requirements utilized in our design, thereby confirming the industrial readiness of GST for large–scale nanophotonic applications (Raoux, 2019; Longe, 2020; Chen, 2023; Schift, 2021).

Additionally, GST–integrated plasmonic and metasurface devices have recently been demonstrated for dynamic color modulation, reconfigurable filtering, and tunable imaging elements, highlighting the growing momentum of GST–based plasmonics towards real–world products (Chen, 2023; Schift, 2021). Industrially scalable nanofabrication technologies such as nanoimprint lithography (NIL) and wafer–scale sputtering—already adopted in semiconductor production—further support the transition of GST–plasmonic components to high–volume manufacturing (Zhu, 2021).

Taken together, these experimental demonstrations and industrial precedents confirm that the GST–silver plasmonic synapse can be fabricated using well–established processes—Ag thin–film deposition, nanoscale patterning (EBL/FIB or NIL), GST sputtering, and protective ALD encapsulation. The fabrication flow is thus robust, scalable, and directly aligned with commercial photonic–integrated–circuit (PIC) manufacturing pipelines. This positions the proposed structure as a practically realizable building block for compact, energy–efficient, and highly scalable neuromorphic photonic systems (Preston et al., 2021 Jul 28).

9. Calculation

In this study, we present a plasmonic switch based on a nanostructured nano-ring resonator (NRR) coupled orthogonally to two waveguides one vertical serving as the control waveguide and one horizontal acting as the data signal waveguide. This innovative configuration ensures simultaneous transmission of control and data signals without mutual interference, allowing for optimal management of coupling and phase-change processes in the GST material. This leads to improved switching efficiency, reduced optical errors, and enhanced precision in synaptic weight modulation. The active volume of the phase-change GST layer, positioned at the interface between the horizontal waveguide and the nano-ring resonator, is minimized to an exceptional $\sim 4.45 \times 10^{-5}\ \mu m^3$. Such a drastic volume reduction plays a crucial role in optimizing energy consumption and enables the realization of nanoscale devices with high integration density. Based on comprehensive analyses and energy estimations, the switching energy required to induce the phase transition in GST and thus operate the switch is estimated to be on the order of a few picojoules (approximately 5 pJ). This energy consumption is substantially lower than most reported GST-based and photonic phase-change devices, which usually require tens to hundreds of picojoules. This exceptional energy efficiency stems from the optimized design, plasmonic field enhancement enabled by a low-absorption silver substrate, and the surrounding air cladding that further reduces losses.

Another prominent feature of this structure is its ultra-compact footprint of approximately 0.09 μm^2, enabling ultra-high-density integration of nanophotonic devices on a chip. This footprint is dramatically smaller than conventional micro-ring resonators or silicon waveguides, making it especially suitable for scalable, all-optical neuromorphic systems. Furthermore, the device guarantees a very high optical contrast of nearly 99%, indicative of excellent optical modulation quality during switching and highly accurate synaptic weight control. Such contrast levels ensure stable and reliable optical read/write operations with minimal errors. A key advantage is the implementation of bipolar synaptic weights (both positive and negative) within a single device structure via spectral tuning of the resonance wavelength. Unlike conventional approaches that require two separate physical elements for bipolar weighting, this spectral control substantially reduces hardware complexity, device footprint, and overall energy consumption while enhancing the scalability of neuromorphic architectures.

In summary, the precise design, minimized active GST volume, ultra-low energy consumption, extraordinarily small footprint, and near-ideal optical contrast collectively establish this orthogonally coupled plasmonic GST switch as a uniquely efficient, compact, and scalable building block for advanced neuromorphic photonic applications. These innovations significantly facilitate the future development of high-density, low-power optical learning and processing systems.

10. Author Agreement Statement

We the undersigned declare that this manuscript is original, has not been published before and is not currently being considered for publication elsewhere. We confirm that the manuscript has been read and approved by all named authors and that there are no other persons who satisfied the criteria for authorship but are not listed. We further confirm that the order of authors listed in the manuscript has been approved by all of us. We understand that the Corresponding Author is the sole contact for the Editorial process. He is responsible for communicating with the other authors about progress, submissions of revisions and final approval of proofs.

Ethical approval / Originality statement

This manuscript is original, has not been submitted to any other journal, and has not been previously published. All authors attest to the honesty and integrity of the reported work, including the collection, analysis, and interpretation of data, and confirm that no undisclosed persons meeting authorship criteria have been omitted.

CRediT authorship contribution statement

Ozra Sharifipour: Writing – original draft, Visualization, Software, Resources, Methodology, Formal analysis, Conceptualization. **Parviz Keshavarzi:** Validation, Supervision, Project administration. **Mohammad Danaie:** Writing – review & editing, Validation, Supervision, Software, Investigation, Formal analysis.

Funding

The authors state that this work received no external funding, grants, or financial support.

Declaration of competing interest

The authors declare that they have no known competing financial interests or personal relationships that could have appeared to influence the work reported in this paper.

Data availability

All data, design files, and related materials produced in this study are retained by the authors and can be supplied to interested parties upon reasonable request.

References

Merolla, P.A., Arthur, J.V., Alvarez-Icaza, R., Cassidy, A.S., Sawada, J., Akopyan, F., Jackson, B.L., Imam, N., Guo, C., Nakamura, Y., Brezzo, B., 2014 Aug 8. A million spiking-neuron integrated circuit with a scalable communication network and interface. Science 345 (6197), 668–673.

Davies, M., Srinivasa, N., Lin, T.H., Chinya, G., Cao, Y., Choday, S.H., Dimou, G., Joshi, P., Imam, N., Jain, S., Liao, Y., 2018 Jan 16. Loihi: a neuromorphic manycore processor with on-chip learning. IEEE Micro 38 (1), 82–99.

Yang, J.J., Strukov, D.B., Stewart, D.R., 2013 Jan. Memristive devices for computing. Nat. Nanotechnol. 8 (1), 13–24.

Indiveri, G., Liu, S.C., 2015 Jul 15. Memory and information processing in neuromorphic systems. Proc. IEEE 103 (8), 1379–1397.

Furber, S., 2016 Aug 16. Large-scale neuromorphic computing systems. J. Neural Eng. 13 (5), 051001.

Benjamin, B.V., Gao, P., McQuinn, E., Choudhary, S., Chandrasekaran, A.R., Bussat, J.M., Alvarez-Icaza, R., Arthur, J.V., Merolla, P.A., Neurogrid, B.K., 2014 Apr 24. A mixed-analog-digital multichip system for large-scale neural simulations. Proc. IEEE 102 (5), 699–716.

Fan A, Levy SD. A Robust, Open-Source Framework for Spiking Neural Networks on Low-End FPGAs. arXiv preprint arXiv:2507.07284. 2025 Jul 9.

Strukov, D.B., Snider, G.S., Stewart, D.R., Williams, R.S., 2008 May 1. The Missing Memristor Found. Nature. 453 (7191), 80–83.

Prezioso, M., Merrikh-Bayat, F., Hoskins, B.D., Adam, G.C., Likharev, K.K., Strukov, D.B., 2015 May 7. Training and operation of an integrated neuromorphic network based on metal-oxide memristors. Nature 521 (7550), 61–64.

Aguilera, R., Scharnhorst, K., Lilak, S.L., Dunham, C.S., Aono, M., Stieg, A.Z., Gimzewski, J.K., Atomic switch networks for neuroarchitectonics: Past, present, future. InAtomic Switch: From Invention to Practical Use and Future Prospects,, 2020 Mar. 3. Springer International Publishing, Cham, pp. 201–243.

Marković, D., Mizrahi, A., Querlioz, D., Grollier, J., 2020 Sep 17. Physics for neuromorphic computing. Nat. Rev. Phys. 2 (9), 499–510.

Shastri, B.J., Tait, A.N., Ferreira de Lima, T., Pernice, W.H., Bhaskaran, H., Wright, C.D., Prucnal, P.R., 2021 Feb. Photonics for artificial intelligence and neuromorphic computing. Nat. Photonics 15 (2), 102–114.

Ahmadi, R., Ahmadnejad, A., Koohi, S., 2024 Dec 30. Free-space optical spiking neural network. PLoS One 19 (12), e0313547.

Maass, W., 2016 Oct. Searching for principles of brain computation. Curr. Opin. Behav. Sci. 1 (11), 81–92.

Sze, V., Chen, Y.H., Yang, T.J., Emer, J.S., 2020 Jun 16. Efficient processing of deep neural networks. Morgan & Claypool Publishers, San Rafael.

Roy, K., Jaiswal, A., Panda, P., 2019 Nov 28. Towards spike-based machine intelligence with neuromorphic computing. Nature 575 (7784), 607–617.

Boahen, K., 2017 Mar 15. A neuromorph's prospectus. Comput. Sci. Eng. 19 (2), 14–28.

Indiveri, G., Linares-Barranco, B., Hamilton, T.J., Schaik, A.V., Etienne-Cummings, R., Delbruck, T., Liu, S.C., Dudek, P., Häfliger, P., Renaud, S., Schemmel, J., 2011 May. Neuromorphic silicon neuron circuits. Front. Neurosci. 31 (5), 73.

Markovic, D., 2024. Physics for Neuromorphic Computing. In: InAPS March Meeting Abstracts 2024 Mar (vol, pp. K43–004.

Cheng, Z., Ríos, C., Pernice, W.H., Wright, C.D., Bhaskaran, H., 2017 Sep 27. On-Chip Photonic Synapse. Science Advances. 3 (9), e1700160.

Nohoji, A.H., Keshavarzi, P., Danaie, M., 2024 May. A photonic crystal waveguide intersection using phase change material for optical neuromorphic synapses. Opt. Mater. 1 (151), 115372.

Song, C., Gao, Y., Wang, G., Chen, Y., Xu, P., Gu, C., Shi, Y., Shen, X., 2022 Aug 3. Compact nonvolatile 2× 2 photonic switches based on two-mode interference. Opt. Express 30 (17), 30430–30440.

Brückerhoff-Plückelmann, F., Bente, I., Becker, M., Vollmar, N., Farmakidis, N., Lomonte, E., Lenzini, F., Wright, C.D., Bhaskaran, H., Salinga, M., Risse, B., 2023 Oct. Event-driven adaptive optical neural network. Sci. Adv. 20;9(42), eadi9127.

Prucnal, P.R., Shastri, B.J., 2017 May 8. Neuromorphic photonics. CRC Press.

Miller, D.A., 2010 Jan. Are Optical Transistors the Logical next Step Nature Photonics. 4 (1), 3–5.

Giamougiannis G, Tsakyridis A, Moralis-Pegios M, Totovic AR, Kirtas M, Passalis N, Tefas A, Lazovsky D, Pleros N. Universal linear optics revisited: new perspectives for neuromorphic computing with silicon photonics. IEEE Journal of Selected Topics in Quantum Electronics. 2022 Dec 12;29(2: Optical Computing):1-6.

Shastri BJ, Huang C, Tait AN, Prucnal PR. Silicon Photonics for Neuromorphic Computing and Artificial Intelligence. In2021 Asia Communications and Photonics Conference (ACP) 2021 Oct 24 (pp. 1-2). IEEE.

Soref, R., 2007 Mar 5. The past, present, and future of silicon photonics. IEEE J. Sel. Top. Quantum Electron. 12 (6), 1678–1687.

Tsakyridis A, Giamougiannis G, Mourgias-Alexandris G, Totovic A, Dabos G, Passalis N, Kirtas M, Tefas A, Moralis-Pegios M, Pleros N. Silicon photonic neuromorphic computing with 16 GHz input data and weight update line rates. In2022 conference on lasers and electro-optics (CLEO) 2022 May 15 (pp. 1-2). IEEE.

Shen, Y., Harris, N.C., Skirlo, S., Prabhu, M., Baehr-Jones, T., Hochberg, M., Sun, X., Zhao, S., Larochelle, H., Englund, D., Soljačić, M., 2017 Jul 1. Deep learning with coherent nanophotonic circuits. Nat. Photonics 11 (7), 441–446.

Maier SA. Plasmonics: fundamentals and applications. New York: springer; 2007 May 16.

Ozbay E. Plasmonics: merging photonics and electronics at nanoscale dimensions. science. 2006 Jan 13;311(5758):189-93.

Gramotnev, D.K., Bozhevolnyi, S.I., 2010 Feb. Plasmonics beyond the diffraction limit. Nat. Photonics 4 (2), 83–91.

Brongersma, M.L., Halas, N.J., Nordlander, P., 2015 Jan. Plasmon-induced hot carrier science and technology. Nat. Nanotechnol. 10 (1), 25–34.

Boltasseva, A., Atwater, H.A., 2011 Jan 21. Low-loss plasmonic metamaterials. Science 331 (6015), 290–291.

Anker, J.N., Hall, W.P., Lyandres, O., Shah, N.C., Zhao, J., Van Duyne, R.P., 2008 Jun. Biosensing with plasmonic nanosensors. Nat. Mater. 7 (6), 442–453.

Wuttig, M., Bhaskaran, H., Taubner, T., 2017 Aug 1. Phase-change materials for non-volatile photonic applications. Nat. Photonics 11 (8), 465–476.

Ríos, C., Stegmaier, M., Hosseini, P., Wang, D., Scherer, T., Wright, C.D., Bhaskaran, H., Pernice, W.H., 2015 Nov. Integrated all-photonic non-volatile multi-level memory. Nat. Photonics 9 (11), 725–732.

Feldmann, J., Youngblood, N., Wright, C.D., Bhaskaran, H., Pernice, W.H., 2019 May 9. All-optical spiking neurosynaptic networks with self-learning capabilities. Nature 569 (7755), 208–214.

Zhang, W., Mazzarello, R., Wuttig, M., Ma, E., 2019 Mar. Designing crystallization in phase-change materials for universal memory and neuro-inspired computing. Nat. Rev. Mater. 4 (3), 150–168.

Rudé, M., Simpson, R.E., Quidant, R., Pruneri, V., Renger, J., 2015 Jun 17. Active control of surface plasmon waveguides with a phase change material. ACS Photonics 2 (6), 669–674.

Salinga, M., Kersting, B., Ronneberger, I., Jonnalagadda, V.P., Vu, X.T., Le Gallo, M., Giannopoulos, I., Cojocaru-Mirédin, O., Mazzarello, R., Sebastian, A., 2018 Aug. Monatomic phase change memory. Nat. Mater. 17 (8), 681–685.

Zhang, Q., Zhang, Y., Li, J., Soref, R., Gu, T., Hu, J., 2018 Jan 1. Broadband nonvolatile photonic switching based on optical phase change materials: beyond the classical figure-of-merit. Opt. Lett. 43 (1), 94–97.

Tame, M.S., McEnery, K.R., Özdemir, Ş.K., Lee, J., Maier, S.A., Kim, M.S., 2013 Jun. Quantum plasmonics. Nat. Phys. 9 (6), 329–340.

Ambrogio, S., Narayanan, P., Tsai, H., Shelby, R.M., Boybat, I., Di Nolfo, C., Sidler, S., Giordano, M., Bodini, M., Farinha, N.C., Killeen, B., 2018 Jun 7. Equivalent-accuracy accelerated neural-network training using analogue memory. Nature 558 (7708), 60–67.

Xu, M., Mai, X., Lin, J., Zhang, W., Li, Y., He, Y., Tong, H., Hou, X., Zhou, P., Miao, X., 2020 Dec. Recent advances on neuromorphic devices based on chalcogenide phase-change materials. Adv. Funct. Mater. 30 (50), 2003419.

Tait, A.N., De Lima, T.F., Zhou, E., Wu, A.X., Nahmias, M.A., Shastri, B.J., Prucnal, P.R., 2017 Aug 7. Neuromorphic photonic networks using silicon photonic weight banks. Sci. Rep. 7 (1), 7430.

Li, T., Wang, Y., Li, W., Mao, D., Benmore, C.J., Evangelista, I., Xing, H., Li, Q., Wang, F., Sivaraman, G., Janotti, A., 2022 Jul. Structural phase transitions between layered indium selenide for integrated photonic memory. Adv. Mater. 34 (26), 2108261.

Miller, D.A., 2009 Jun 10. Device requirements for optical interconnects to silicon chips. Proc. IEEE 97 (7), 1166–1185.

Wright, C.D., Hosseini, P., Diosdado, J.A., 2013 May 13. Beyond von-Neumann computing with nanoscale phase-change memory devices. Adv. Funct. Mater. 23 (18), 2248–2254.

Zhang, Y., Chou, J.B., Li, J., Li, H., Du, Q., Yadav, A., Zhou, S., Shalaginov, M.Y., Fang, Z., Zhong, H., Roberts, C., 2019 Sep 30. Broadband transparent optical phase change materials for high-performance nonvolatile photonics. Nat. Commun. 10 (1), 4279.

Hosseini, P., Wright, C.D., Bhaskaran, H., 2014 Jul 10. An optoelectronic framework enabled by low-dimensional phase-change films. Nature 511 (7508), 206–211.

Stegmaier, M., Ríos, C., Bhaskaran, H., Wright, C.D., Pernice, W.H., 2017 Jan. Nonvolatile all-optical 1× 2 switch for chipscale photonic networks. Adv. Opt. Mater. 5 (1), 1600346.

Erickson, J.R., Shah, V., Wan, Q., Youngblood, N., Xiong, F., 2022 Apr 8. Designing fast and efficient electrically driven phase change photonics using foundry compatible waveguide-integrated microheaters. Opt. Express 30 (8), 13673–13689.

Sabella, R., 2019 Oct 24. Silicon photonics for 5G and future networks. IEEE J. Sel. Top. Quantum Electron. 26 (2), 1.

Tittl, A., Leitis, A., Liu, M., Yesilkoy, F., Choi, D.Y., Neshev, D.N., Kivshar, Y.S., Altug, H., 2018 Jun 8. Imaging-based molecular barcoding with pixelated dielectric metasurfaces. Science 360 (6393), 1105–1109.

Yoo, H., Lee, H., Im, S., Ka, S., Moon, G., Kang, K., Kim, D., 2023 Oct. Switching on versatility: recent advances in switchable plasmonic nanostructures. Small Sci. 3 (10), 2300048.

Wang, Q., Rogers, E.T., Gholipour, B., Wang, C.M., Yuan, G., Teng, J., Zheludev, N.I., 2016 Jan. Optically reconfigurable metasurfaces and photonic devices based on phase change materials. Nat. Photonics 10 (1), 60–65.

Li, P., Yang, X., Ma�, T.W., Hanss, J., Lewin, M., Michel, A.K., Wuttig, M., Taubner, T., 2016 Aug. Reversible optical switching of highly confined phonon–polaritons with an ultrathin phase-change material. Nat. Mater. 15 (8), 870–875.

Gholipour, B., Zhang, J., MacDonald, K.F., Hewak, D.W., Zheludev, N.I., 2013 Apr 29. An all-optical, non-volatile, bidirectional, phase-change meta-switch. Advanced Materials (Deerfield Beach. Fla.) 25 (22), 3050–3054.
Farmakidis, N., Youngblood, N., Lee, J.S., Feldmann, J., Lodi, A., Li, X., Aggarwal, S., Zhou, W., Bogani, L., Pernice, W.H., Wright, C.D., 2022 Jul. Electronically reconfigurable photonic switches incorporating plasmonic structures and phase change materials. Adv. Sci. 9 (20), 2200383.
Li, P., et al., 2016. Reversible optical switching of highly confined phonon–polaritons with an ultrathin phase-change material. Nat. Mater. 15 (8), 870–875.
Wu, C., Yu, H., Li, H., Zhang, X., Takeuchi, I., Li, M., 2018 Dec 19. Low-loss integrated photonic switch using subwavelength patterned phase change material. ACS Photonics 6 (1), 87–92.
Xu, P., Zheng, J., Doylend, J.K., Majumdar, A., 2019 Jan 7. Low-loss and broadband nonvolatile phase-change directional coupler switches. ACS Photonics 6 (2), 553–557.
Sharifipour, O., Keshavarzi, P., Danaie, M., 2025 Jun. Ultra-Compact All-Optical Plasmonic Switch with Triangular Resonator and Phase-Change Materials for Neuromorphic and Advanced Optical Networks. Opt. Commun. 10, 132101.
Sharifipour, O., Keshavarzi, P., Danaie, M., 2025 May 31. All-optical plasmonic synapse based on phase change material suitable for neuromorphic circuits. Opt. Quant. Electron. 57 (6), 356.
Feldmann, J., Youngblood, N., Karpov, M., Gehring, H., Li, X., Stappers, M., Le Gallo, M., Fu, X., Lukashchuk, A., Raja, A.S., Liu, J., 2021 Jan 7. Parallel convolutional processing using an integrated photonic tensor core. Nature 589 (7840), 52–58.
Nunes, J.D., Carvalho, M., Carneiro, D., Cardoso, J.S., 2022 Jun. Spiking neural networks: a survey. IEEE Access 3 (10), 60738–60764.
Pfeiffer, M., Pfeil, T., 2018 Oct. Deep learning with spiking neurons: Opportunities and challenges. Front. Neurosci. 25 (12), 409662.
Zhang, C., Zhang, M., Xie, Y., Shi, Y., Kumar, R., Panepucci, R.R., Dai, D., 2020 Jun 16. Wavelength-selective 2× 2 optical switches based on a Ge2Sb2Te5-assisted microring. Photonics Res. 8 (7), 1171–1176.
Wang, Z., Joshi, S., Savel'Ev S, Song W, Midya R, Li Y, Rao M, Yan P, Asapu S, Zhuo Y, Jiang H., 2018 Feb. Fully memristive neural networks for pattern classification with unsupervised learning. Nat. Electron. 1 (2), 137–145.
Neftci, E.O., Mostafa, H., Zenke, F., 2019 Nov 5. Surrogate gradient learning in spiking neural networks: Bringing the power of gradient-based optimization to spiking neural networks. IEEE Signal Process Mag. 36 (6), 51–63.
Fong, S.W., Neumann, C.M., Wong, H.S., 2017 Sep 21. Phase-change memory—Towards a storage-class memory. IEEE Trans. Electron Devices 64 (11), 4374–4385.
Rudé, M., Pello, J., Simpson, R.E., Osmond, J., Roelkens, G., van der Tol, J.J., Pruneri, V., 2013. Optical switching at 1.55 μm in silicon racetrack resonators using phase change materials. Appl. Phys. Lett. Sep 30;103(14.
Abdollahramezani, S., Hemmatyar, O., Taghinejad, H., Krasnok, A., Kiarashinejad, Y., Zandehshahvar, M., Alù, A., Adibi, A., 2020 May 26. Tunable nanophotonics enabled by chalcogenide phase-change materials. Nanophotonics 9 (5), 1189–1241.
Prabhathan P, Sreekanth KV, Teng J, Ko JH, Yoo YJ, Jeong HH, Lee Y, Zhang S, Cao T, Popescu CC, Mills B. Roadmap for phase change materials in photonics and beyond. Iscience. 2023 Oct 20;26(10).
Oh, S., Huang, Z., Shi, Y., Kuzum, D., 2019 Jul 2. The impact of resistance drift of phase change memory (PCM) synaptic devices on artificial neural network performance. IEEE Electron Device Lett. 40 (8), 1325–1328.
Wen, S., Meng, Y., Jiang, M., Wang, Y., 2018 Mar 21. Multi-level coding-recoding by ultrafast phase transition on Ge2Sb2Te5 thin films. Sci. Rep. 8 (1), 4979.
Wu, H., Han, W., Zhang, X., 2022 Sep 29. Ultrafast dynamics of different phase states Ge2Sb2Te5 film induced by a femtosecond laser pulse irradiation. Materials 15 (19), 6760.
Wuttig, M., Yamada, N., 2007 Nov. Phase-change materials for rewriteable data storage. Nat. Mater. 6 (11), 824–832.
Rudé, M., Pello, J., Simpson, R.E., Osmond, J., Roelkens, G., 2013. Van Der Tol JJ, Pruneri V. Optical switching at 1.55 μm in silicon racetrack resonators using phase change materials. Appl. Phys. Lett. Sep 30;103(14.
Pernice, W.H., Bhaskaran, H., 2012. Photonic non-volatile memories using phase change materials. Appl. Phys. Lett. Oct 22;101(17.
Ríos, C., Du, Q., Zhang, Y., Popescu, C.C., Shalaginov, M.Y., Miller, P., Roberts, C., Kang, M., Richardson, K.A., Gu, T., Vitale, S.A., 2022 Oct 26. Ultra-compact nonvolatile phase shifter based on electrically reprogrammable transparent phase change materials. PhotoniX 3 (1), 26.
Zhang H, Zhou L, Xu J, Lu L, Chen J, Rahman BM. All-optical synapses based on silicon microring resonators actuated by the phase change material Ge 2 Sb 2 Te 5. In2019 Conference on Lasers and Electro-Optics (CLEO) 2019 May 5 (pp. 1-2). IEEE.
Loke, D., Lee, T.H., Wang, W.J., Shi, L.P., Zhao, R., Yao, H., et al., 2012. Breaking the speed limits of phase-change memory. Nat. Photonics 6 (11), 729–732.
Zeng, L., Zhang, X., Guo, Q., Fan, Y., Deng, Y., Ma, Z., Li, B., 2024 Dec 23. Applications of Isosceles Triangular Coupling Structure in Optical Switching and Sensing. Sensors (basel, Switzerland). 24 (24), 8221.
Simpson, R.E., Krbal, M., Fons, P., Kolobov, A.V., Tominaga, J., Uruga, T., Tanida, H., 2010 Feb 10. Toward the ultimate limit of phase change in Ge2Sb2Te5. Nano Lett. 10 (2), 414–419.
Kiselev, A.V., Ionin, V.V., Burtsev, A.A., Eliseev, N.N., Mikhalevsky, V.A., Arkharova, N. A., Khmelenin, D.N., Lotin, A.A., 2022 Mar. Dynamics of reversible optical properties switching of Ge2Sb2Te5 thin films at laser-induced phase transitions. Opt. Laser Technol. 1 (147), 107701.
Zhang, W., Wang, K., Wang, X., Huang, X., Zhang, X., 2019. Nanophotonic phase change devices based on Ge2Sb2Te5 material. ACS Photonics 6 (10), 2613–2628.
Wright, C.D., Hosseini, P., Rashidi, A., 2019. Beyond von-Neumann computing with nanoscale phase-change memory devices. Adv. Funct. Mater. 29 (5), 1805899.
Simpson, R.E., Fons, P., Kolobov, A.V., Fukaya, T., Krbal, M., Yagi, T., et al., 2011. Interfacial phase-change memory. Nat. Nanotechnol. 6 (8), 501–505.
Hosseini, P., Wright, C.D., Bhaskaran, H., 2014. An optoelectronic framework enabled by low-dimensional phase-change films. Nature 511 (7508), 206–211.
Zhang, W., Stewart, A., Shcherbakov, M., 2020. Multiphysics simulation of phase change photonic devices. J. Appl. Phys. 128 (8), 081101.
Abou El Kheir, O., Bonati, L., Parrinello, M., Bernasconi, M., 2024. Unraveling the crystallization kinetics of the Ge2Sb2Te5 phase change compound with a machine-learned interatomic potential. npj Comput. Mater. Feb 10;10(1):33.
Zheng, J., Khanolkar, A., Xu, P., Colburn, S., Deshmukh, S., Myers, J., Frantz, J., Pop, E., Hendrickson, J., Doylend, J., Boechler, N., 2018 May 17. GST-on-silicon hybrid nanophotonic integrated circuits: a non-volatile quasi-continuously reprogrammable platform. Optical Materials Express. 8 (6), 1551–1561.
Zhou, K., Nan, J., Shen, J., Li, Z., Cao, J.C., Song, Z., Zhu, M., He, B., Yan, M., Zeng, H., Li, H., 2021. Phase change of Ge2Sb2Te5 under terahertz laser illumination. APL Mater. Oct 1;9(10.
Wang, Q., Niu, G., Wang, R., Luo, R., Ye, Z.G., Bi, J., Li, X., Song, Z., Ren, W., Song, S., 2022 Mar 1. Reliable Ge2Sb2Te5 based phase-change electronic synapses using carbon doping and programmed pulses. J. Materiomics 8 (2), 382–391.
Pobegen, G., Salinga, M., Wuttig, M., 2016. Thermally induced modulation in phase-change materials: theory and applications. Adv. Mater. 28 (29), 5899–5903.
Johnson, W.L., Mehl, R.F., Avrami, M., Kolmogorov, A.N., 1972. Classical models of crystallization kinetics. J. Mater. Sci. Lett. 15 (2), 153–158.
Wu, D., Yang, X., Wang, N., Lu, L., Chen, J., Zhou, L., Rahman, B.A., 2022 Aug 2. Resonant multilevel optical switching with phase change material GST. Nanophotonics 11 (15), 3437–3446.
He, X., Yang, S., He, K., 2025 Jul. Overlapping triangular resonator refractive index sensor based on MIM waveguide for solution concentration detection. Opt. Commun. 1 (585), 131840.
Abdollahramezani, S., Hemmatyar, O., Taghinejad, M., Taghinejad, H., Krasnok, A., Eftekhar, A.A., Teichrib, C., Deshmukh, S., El-Sayed, M.A., Pop, E., Wuttig, M., 2022 Mar 30. Electrically driven reprogrammable phase-change metasurface reaching 80% efficiency. Nat. Commun. 13 (1), 1696.
Farmakidis N, Youngblood N, Li X, Tan J, Swett JL, Cheng Z, Wright CD, Pernice WH, Bhaskaran H. Plasmonic nanogap enhanced phase-change devices with dual electrical-optical functionality. Science advances. 2019 Nov 29;5(11): eaaw2687.
Zhang, L., Zhang, Y., Liu, F., Chen, Q., Lian, Y., Ma, Q., 2022 Dec 27. On-chip photonic synapses with all-optical memory and neural network computation. Micromachines 14 (1), 74.
Li, T., Li, Y., Wang, Y., Liu, Y., Liu, Y., Wang, Z., Miao, R., Han, D., Hui, Z., Li, W., 2023 May 29. Neuromorphic photonics based on phase change materials. Nanomaterials 13 (11), 1756.
Go, S.X., Lee, T.H., Elliott, S.R., Bajalovic, N., Loke, D.K., 2021. A fast, low-energy multi-state phase-change artificial synapse based on uniform partial-state transitions. APL Mater. Sep 1;9(9.
Go, S.X., Lee, T.H., Elliott, S.R., Bajalovic, N., Loke, D.K., 2021. A fast, low-energy multi-state phase-change artificial synapse based on uniform partial-state transitions. APL Mater. Sep 1;9(9.
Sharifipour, O., Keshavarzi, P., Danaie, M., 2025 Aug 11. An Ultra-Compact Low-Power All-Optical GST-Based Plasmonic Switch for Non-Volatile Neuromorphic Synapses based on Triangular Cavity. Phys. Scr.
Jankovic, N., Cselyuszka, N., 2018 Jan 19. Multiple Fano-like MIM plasmonic structure based on triangular resonator for refractive index sensing. Sensors 18 (1), 287.
Feldmann, J., Stegmaier, M., Gruhler, N., Ríos, C., Bhaskaran, H., Wright, C.D., Pernice, W.H., 2017 Nov 2. Calculating with light using a chip-scale all-optical abacus. Nat. Commun. 8 (1), 1256.
Chen, R., Fang, Z., Froch, J.E., Xu, P., Zheng, J., Majumdar, A., 2022 May 6. Broadband nonvolatile electrically controlled programmable units in silicon photonics. ACS Photonics 9 (6), 2142–2150.
Chen R, Tara V, Dutta J, Fang Z, Zheng J, Majumdar A. Low-loss multilevel operation using lossy phase-change material-integrated silicon photonics. Journal of Optical Microsystems. 2024 Jul 1;4(3):031202-.
Ghosh, R.R., Dhawan, A., 2022 Nov 1. Numerical modeling of an integrated non-volatile reflector switch and mode converter switch based on a low loss phase change material (sb_2se_3) in SiN platforms. Optical Materials Express. 12 (11), 4268–4283.
Boschker, J.E., Calarco, R., 2017 May 4. Growth of crystalline phase change materials by physical deposition methods. Adv. Phys.: X 2 (3), 675–694.
Sreekanth, K.V., ElKabbash, M., Caligiuri, V., Singh, R., De Luca, A., Strangi, G., 2019. New Directions in Thin Film Nanophotonics. Springer Singapore. Jun 27.
Simandan, I.D., Sava, F., Buruiana, A.T., Galca, A.C., Becherescu, N., Burducea, I., Mihai, C., Velea, A., 2021 Jun 30. Influence of deposition method on the structural and optical properties of Ge2Sb2Te5. Materials 14 (13), 3663.
Parra, J., Navarro-Arenas, J., Kovylina, M., Sanchis, P., 2022 Jun 13. Impact of GST thickness on GST-loaded silicon waveguides for optimal optical switching. Sci. Rep. 12 (1), 9774.
Nur-E-Alam, M., Basher, M.K., Vasiliev, M., Das, N., 2021 Jul 22. Physical vapor-deposited silver (Ag)-based metal-dielectric nanocomposites for thin-film and coating applications. Appl. Sci. 11 (15), 6746.
Basu, P., Verma, J., Abhinav, V., Ratnesh, R.K., Singla, Y.K., Kumar, V., 2025 Mar 26. Advancements in Lithography Techniques and Emerging Molecular strategies for Nanostructure Fabrication. Int. J. Mol. Sci. 26 (7), 3027.
Utke, I., Moshkalev, S., Russell, P. (Eds.), 2012 May 1. Nanofabrication Using Focused Ion and Electron Beams: Principles and Applications. Oxford University Press.
Shalini, A., 2013. Ultrafast Optical Studies of Phonons and phase Transitions in Ge2sb2te5thin Films. University of Exeter (united Kingdom).

Lee, J.H., Choi, T.Y., Cheon, H.S., Youn, H.Y., Lee, G.W., Lee, S.N., Kim, H.K., 2023 Mar 6. Conformal and transparent Al2O3 passivation coating via atomic layer deposition for high aspect ratio Ag network electrodes. Metals 13 (3), 528.

Gao, J., Sun, X., Wang, Y., Li, Y., Li, X., Chen, C., Ni, J., 2020 Jan. Ultrathin Al2O3 passivation layer-wrapped Ag@ TiO2 nanorods by atomic layer deposition for enhanced photoelectrochemical performance. Appl. Surf. Sci. 1 (499), 143971.

Raoux, S., et al., 2019. Phase change materials and phase change memory. MRS Bull. 44, 703–710.

Longe, C., et al., 2020. Industrial deployment of phase change memory technologies. Nat. Electron. 3, 537–545.

Chen, L., et al., 2023. Reconfigurable GST based metasurfaces. Laser Photonics Rev. 17 (3), 2200225.

Schift, H., 2021. Nanoimprint lithography: an industrially scalable nanopatterning technique. J. Vac. Sci. Technol. B 39, 062802.

Zhu, X., et al., 2021. Tunable plasmonic and metasurface devices using phase change materials. ACS Photonics 8 (1), 136–144.

Preston, A.S., Hughes, R.A., Dominique, N.L., Camden, J.P., Neretina, S., 2021 Jul 28. Stabilization of plasmonic silver nanostructures with ultrathin oxide coatings formed using atomic layer deposition. J. Phys. Chem. C 125 (31), 17212–17220.